Electron Energy Partition across Interplanetary Shocks. I. Methodology and Data Product

Lynn B. Wilson III[1] , Li-Jen Chen[1] , Shan Wang[1,2] , Steven J. Schwartz[3] , Drew L. Turner[4] , Michael L. Stevens[5] , Justin C. Kasper[6] , Adnane Osmane[7] , Damiano Caprioli[8] , Stuart D. Bale[9] , Marc P. Pulupa[9] , Chadi S. Salem[9] , and Katherine A. Goodrich[9]

[1] NASA Goddard Space Flight Center, Heliophysics Science Division, Greenbelt, MD, USA; lynn.b.wilsoniii@gmail.com
[2] Astronomy Department, University of Maryland, College Park, Maryland, USA
[3] Laboratory for Atmospheric and Space Physics, University of Colorado, Boulder, Boulder, CO, USA
[4] Space Sciences Department, The Aerospace Corporation, El Segundo, CA, USA
[5] Harvard-Smithsonian Center for Astrophysics, Harvard University, Cambridge, MA, USA
[6] University of Michigan, Ann Arbor, School of Climate and Space Sciences and Engineering, Ann Arbor, MI, USA
[7] Department of Physics, University of Helsinki, Helsinki, Finland
[8] Department of Astronomy and Astrophysics, University of Chicago, Chicago, IL, USA
[9] University of California Berkeley, Space Sciences Laboratory, Berkeley, CA, USA

Abstract

Analyses of 15,314 electron velocity distribution functions (VDFs) within $\pm 2\,\mathrm{hr}$ of 52 interplanetary (IP) shocks observed by the *Wind* spacecraft near 1 au are introduced. The electron VDFs are fit to the sum of three model functions for the cold dense core, hot tenuous halo, and field-aligned beam/strahl component. The best results were found by modeling the core as either a bi-kappa or a symmetric (or asymmetric) bi-self-similar VDF, while both the halo and beam/strahl components were best fit to bi-kappa VDF. This is the first statistical study to show that the core electron distribution is better fit to a self-similar VDF than a bi-Maxwellian under all conditions. The self-similar distribution deviation from a Maxwellian is a measure of inelasticity in particle scattering from waves and/or turbulence. The ranges of values defined by the lower and upper quartiles for the kappa exponents are $\kappa_{ec} \sim 5.40\text{--}10.2$ for the core, $\kappa_{eh} \sim 3.58\text{--}5.34$ for the halo, and $\kappa_{eb} \sim 3.40\text{--}5.16$ for the beam/strahl. The lower-to-upper quartile range of symmetric bi-self-similar core exponents is $s_{ec} \sim 2.00\text{--}2.04$, and those of asymmetric bi-self-similar core exponents are $p_{ec} \sim 2.20\text{--}4.00$ for the parallel exponent and $q_{ec} \sim 2.00\text{--}2.46$ for the perpendicular exponent. The nuanced details of the fit procedure and description of resulting data product are also presented. The statistics and detailed analysis of the results are presented in Paper II and Paper III of this three-part study.

Key words: methods: numerical – methods: statistical – plasmas – shock waves – solar wind – Sun: coronal mass ejections (CMEs)

1. Background and Motivation

The solar wind is an ionized gas experiencing collective effects where Coulomb collisions occur, but the rates are often so low that, for instance, two constituent particle species, s' and s, are not in thermodynamic or thermal equilibrium, i.e., $(T_{s'}/T_s)_{\mathrm{tot}} \neq 1$ for $s' \neq s$, and the relevant scale lengths are orders of magnitude smaller than the collisional mean free path (e.g., Wilson et al. 2018). Therefore, for any process dependent on scales like the thermal gyroradii, ρ_{cs}, or inertial lengths, λ_s, the media is considered collisionless (see Appendix A for definitions). That the solar wind is a nonequilibrium, weakly collisional, kinetic gas results in multicomponent velocity distribution functions (VDFs) for both ions (e.g., Kasper et al. 2006, 2012, 2013; Maruca et al. 2011; Maruca & Kasper 2013; Wicks et al. 2016) and electrons (e.g., Schwartz & Marsch 1983; Maksimovic et al. 1997, 1998; Lin 1998; Pierrard et al. 1999, 2001; Štverák et al. 2008, 2009; Pulupa et al. 2014a).
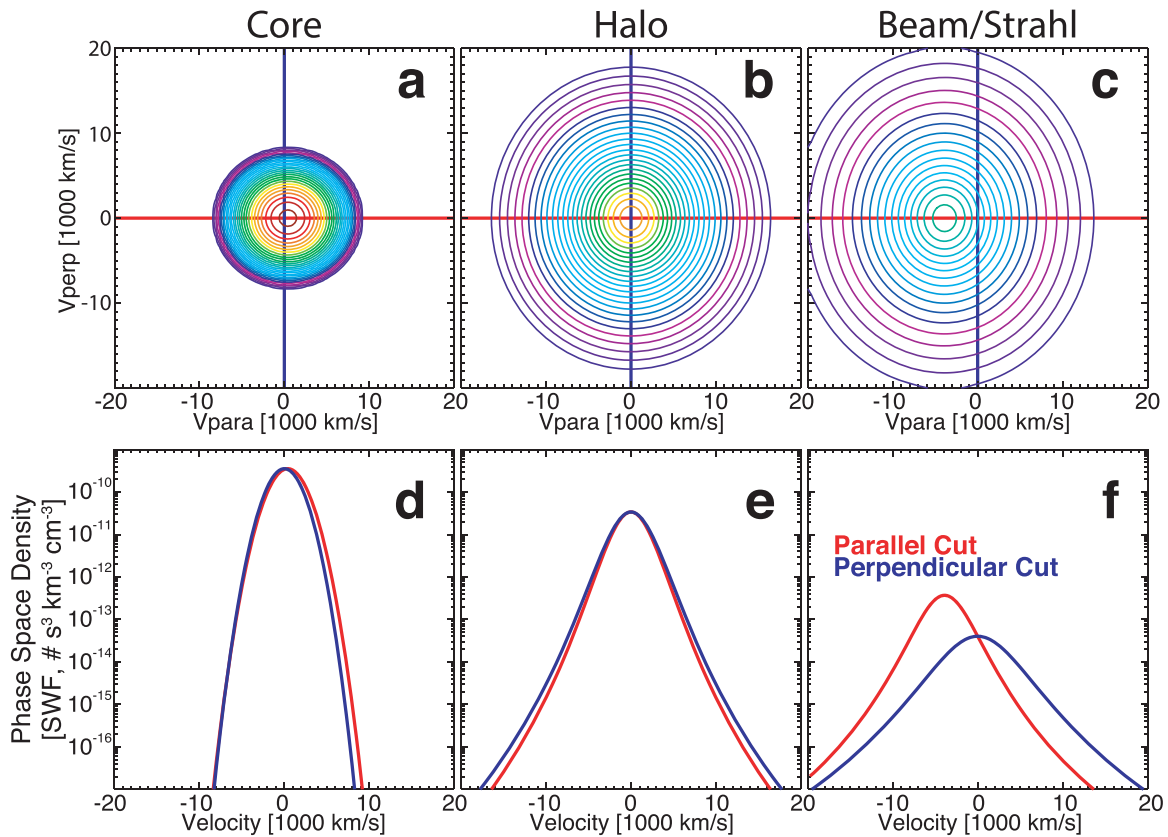
The electron VDFs in the solar wind below $\sim 1\,\mathrm{keV}$ are composed of a cold core with energies $E_{ec} \lesssim 15\,\mathrm{eV}$ (e.g.,

Pilipp et al. 1987a, 1987b, 1987c, 1990; Maksimovic et al. 1997, 1998; Bale et al. 2013; Pulupa et al. 2014a), a hot, tenuous halo with $E_{eh} \gtrsim 20\,\mathrm{eV}$ (e.g., Maksimovic et al. 1997, 1998; Štverák et al. 2008, 2009; Pulupa et al. 2014a), and an antisunward, field-aligned beam called the strahl with $E_{eb} \sim$ a few tens of eV (e.g., Crooker et al. 2003; Štverák et al. 2009; Bale et al. 2013; Graham et al. 2017, 2018; Horaites et al. 2018; see, e.g., Figure 1 for an illustrative example). The electrons also dominate the solar wind heat flux (e.g., Crooker et al. 2003; Pagel et al. 2005, 2007; Bale et al. 2013), arising from the consistent skewness in the VDFs, specifically the halo and/or strahl components. Note that there also exists a suprathermal superhalo with $E_{esh} \gtrsim 1\,\mathrm{keV}$ (e.g., Lin 1998; Wang et al. 2012, 2015), but these higher-energy electrons are not examined herein.

The three electron components below $\sim 1\,\mathrm{keV}$ are predicted and observed to be coupled through multiple processes from wave–particle interactions (e.g., Phillips et al. 1989a, 1989b; Vocks & Mann 2003; Vocks et al. 2005; Saito & Gary 2007; Saito et al. 2008; Pierrard et al. 2011, 2016; Yoon et al. 2012, 2015, 2016; Yoon 2014) to adiabatic transport effects (e.g., Schwartz & Marsch 1983) to collisional effects (e.g., Schwartz & Marsch 1983; Pilipp et al. 1987a, 1987b, 1987c). They have also been shown to behave differently across collisionless

Figure 1. Illustrative example VDFs of the core, halo, and beam/strahl components of the electron VDFs in the solar wind near 1 au. The top row (panels (a) through (c)) shows contours of constant phase-space density (cm^{-3} km^{-3} s^{+3}) of a two-dimensional cut through a three-dimensional VDF. The plane and coordinate basis are defined by the quasi-static magnetic field, B_o, and the ion bulk flow velocity, V_i. The vertical axis is defined by the unit vector $(B_o \times V_i) \times B_o$ and the horizontal axis by B_o. The bottom row (panels (d) through (f)) shows one-dimensional cuts of the VDF along the horizontal (solid red line) and along the vertical (solid blue line). The locations of these cuts are defined by the color-coded crosshairs in the top row of panels. The VDF is shown in the ion bulk flow rest frame.

shocks depending on shock strength (e.g., Wilson et al. 2009, 2010).

An illustrative example, showing the three electron components typically observed in the solar wind near 1 au below ~1.2 keV, is shown in Figure 1. The component parameters are exaggerated[10] for illustrative purposes but are based on the fit results of the VDF shown in Figure 4. The core is modeled by a symmetric bi-self-similar VDF and the halo and beam/strahl by a bi-kappa VDF (see Section 3.1). In this case, the self-similar exponent reduced to 2, so the VDF reduced to a qbi-Maxwellian (see Section 3.1). This example is phenomenologically consistent with the majority of solar wind electron VDFs (e.g., Pilipp et al. 1987a, 1987b, 1987c; Phillips et al. 1989a, 1989b; Štverák et al. 2008, 2009).

Despite its collisionless, nonequilibrium nature, the solar wind can support the existence of shock waves. That the particles are in neither thermal nor thermodynamic equilibrium leads to a nonhomogeneous partition of energy not only among electrons and ions but also among the components of each species, e.g., the core electrons do not have the same response as the halo to collisionless shock waves. The reason for the nonhomogeneous partition of energy lies in the energy-dependent mechanisms that transfer the bulk flow kinetic energy lost across the shock ramp to other forms like heat or particle acceleration (see,

e.g., Coroniti 1970; Tidman & Krall 1971; Sagdeev 1966; Kennel et al. 1985; Treumann 2009; Wilson 2016; Wilson et al. 2017, and references therein). The mechanisms can also be dependent on pitch angle and species (e.g., Sagdeev 1966; Artemyev et al. 2013, 2014, 2015, 2016, 2017a, 2017b, 2018). Most collisionless shocks are subsonic to electrons, yet electrons still respond to the shock, showing even Mach-number-dependent effects (e.g., Feldman et al. 1982, 1983a, 1983b; Thomsen et al. 1985, 1987, 1993; Wilson et al. 2010; Masters et al. 2011). This is all further complicated by recent observations showing that the evolution of the electron VDF through a collisionless shock is not a trivial, uniform inflation of the entire distribution but a multistage process that deforms and redistributes/exchanges energy for different energies and pitch angles at different stages (e.g., Chen et al. 2018; Goodrich et al. 2018, 2019). There is no currently known way to quantify these nonhomogenous changes to capture the energy- and pitch-angle-dependent effects; therefore, the next best systematic approach for a statistical study is to parameterize the electron components by their velocity moments. This is further supported by the fact that nearly all theories describing the evolution of electron VDFs rely on either the velocity moments or a model VDF (e.g., Schunk 1975, 1977; Schwartz & Marsch 1983; Schwartz et al. 1988; Livadiotis 2015, 2017; Nicolaou et al. 2018; Shizgal 2018).

In this first part of a multipart study we describe the methodology and numerical analysis techniques used to model the solar wind eVDFs below ~1.2 keV observed by the *Wind*

---

[10] The following were enhanced to increase contrast and for ease of viewing differences: parallel core temperature, perpendicular halo temperature, and parallel core drift speed.

spacecraft near 1 au around 52 interplanetary (IP) shocks. This is the first statistical study to show that the core electron distribution is better fit to a self-similar VDF than a bi-Maxwellian under all conditions. The analysis differs from numerous previous studies in its approach and the model functions used, each of which is justified herein using physically significant arguments. A benefit of the analysis is an improved, semianalytic relationship between the spacecraft potential and ion number density. The paper also includes procedural documentation to disclose the nuances and issues associated with applying a nonlinear least-squares fitting algorithm to in situ VDF data in the solar wind. This serves as a reference for use of the resulting data product described herein. In Paper II (Wilson et al. 2019a) the statistical results of the model fits are presented with comparison to previous studies and associated discussions. In Paper III (Wilson et al. 2019b) the analysis and interpretation of the model fit results are presented.

This paper is outlined as follows: Section 2 introduces the data sets and event selection; Section 3 introduces the methodology of the fit analysis, model functions, parameter constraints, quality control, and summary of fit results; Section 4 discusses the statistics of the fit exponents and drift velocities; and Section 5 discusses the results and interpretations with reference to further analysis in the following Papers II and III. Appendices are also included to provide additional details of the parameter definitions (Appendix A), spacecraft potential and detector calibration (Appendix B), numerical analysis procedure (Appendix C), numerical instabilities (Appendix D), direct fit method comparisons (Appendix E), and the data product produced by this effort (Appendix F).

2. Data Sets and Event Selection

In this section we introduce the instrument data sets and shock database used to examine the data observed by the *Wind* spacecraft (Harten & Clark 1995) near 1 au. The data described herein spanned from 00:55:40 UTC on 1995 February 26 to 23:04:00 UTC on 2000 February 20. Additional supplemental material, including a PDF file containing the list of interplanetary shock event dates with associated parameters, shock parameter definitions, shock normal technique definitions, additional statistics in the form of histograms, and additional information about the model VDFs used herein, can be found at [doi:10.5281/zenodo.2875806] (Wilson et al. 2019c). The supplemental material also includes two ASCII files of fit results described in Appendix F. The symbol/parameter definitions are found in Appendix A.

Quasi-static magnetic field vectors ($\boldsymbol{B}_o$) were measured by the *Wind*/MFI dual, triaxial fluxgate magnetometers (Lepping et al. 1995) using the 3 s cadence data for each particle distribution. The components/directions of some parameters are defined with respect to $\boldsymbol{B}_o$ using the subscript j. That is, the parallel ($j = \parallel$) and the perpendicular components ($j = \perp$) of any vector or pseudo-tensor (e.g., temperature) are defined with respect to $\boldsymbol{B}_o$.

The electron VDFs were measured by the *Wind*/3DP low-energy (i.e., few eV to $\sim$1.2 keV) electron electrostatic analyzer (Lin et al. 1995) or EESA Low. The instrument operated in both burst and survey modes for the data presented herein, which have cadences of $\sim$3 s and $\sim$24–78 s, respectively. The energy and angular resolutions are command-able, but the instrument typically operates with $\Delta E / E \sim 20\%$

and $\Delta \phi \sim 5^{\circ}$–$22^{\circ}\!.5$ depending on the poloidal anode[11] (see, e.g., Wilson et al. 2009, 2010, for instrument details).

The EESA Low measurements are contaminated with photoelectrons from the spacecraft, something that must be accounted for to obtain accurate velocity moments or any other results. The details of how the spacecraft potential, ϕ_{sc}, was numerically determined for each VDF are described in Appendix B. The VDFs are transformed into the ion frame prior to any fit using relativistically correct Lorentz transformations, where the steps are as follows: (1) convert the units of the VDFs to phase-space density ($\#\ \mathrm{cm}^{-3}\,\mathrm{s}^{+3}\,\mathrm{km}^{-3}$), (2) correct the energies by ϕ_{sc}, (3) convert the energy-angle bins to velocity coordinates, and (4) transform the velocities into the ion rest frame using proper Lorentz transformations. Nothing need be done to VDFs once in units of phase-space density, as phase-space density is a Lorentz invariant (Van Kampen 1969) (see Appendices B and C for details).

We also examined solar wind proton and alpha-particle velocity moments determined by a nonlinear least-squares fitting algorithm (e.g., Kasper et al. 2006; Maruca & Kasper 2013) observed by the *Wind*/SWE Faraday cups (Ogilvie et al. 1995). Similar quality requirements for the SWE results to those discussed in Wilson et al. (2018) were used herein.

The VDFs examined are found within ± 2 hr of 52 IP shocks found in the *Wind* shock database from the Harvard Smithsonian Center for Astrophysics.[12] Of those 52 IP shocks, there were 16 quasi-parallel ($\theta_{Bn} \leqslant 45^{\circ}$), 36 quasi-perpendicular ($\theta_{Bn} > 45^{\circ}$), 45 low Mach number ($\langle M_f \rangle_{\mathrm{up}} < 3$), and 7 high Mach number ($\langle M_f \rangle_{\mathrm{up}} \geqslant 3$) shocks. The shock parameters for the 52 IP shocks examined in this three-part set of papers are shown in Table 1 (see, e.g., Wilson et al. 2019c, for a full list of values for each shock). The IP shocks examined were selected because of burst mode 3DP availability. See Appendix A for definitions of symbols and/or parameters.

3. Fit Methodology

This section (and Appendix C) introduces and discusses the nuances of the approach and software used to numerically compute the model fit parameters for every electron VDF examined. The nuances and details are provided for reproducibility and documentation for the data product discussed in Appendix F.

The data are fit to a user-defined model function using a nonlinear least-squares fitting algorithm called the Levenberg–Marquardt algorithm (LMA; Moré 1978). The generalized LMA software used for the present study is called MPFIT (Markwardt 2009). The specific details for its use are outlined in Appendix C.

The components of the electron VDFs are fit to bi-Maxwellian, bi-kappa, or bi-self-similar model functions (see Section 3.1). The components can be fit separately because the solar wind is a nonequilibrium, weakly collisional, kinetic gas. That is, in the absence of a magnetic field, each electron component could, in principle, stream past the other components for nearly an astronomical unit without significant interaction. Thus, there is physical justification to fit to the sum of three model functions (see Appendix C for details).

Given that the bi-self-similar reduces to the bi-Maxwellian in the limit as the exponential argument goes to 2 and that it

---

[11] The ecliptic plane bins have higher angular resolution than the zenith.
[12] https://www.cfa.harvard.edu/shocks/wi_data/

Table 1
Shock Parameters

Parameter	$X_{\min}$ [a]	$X_{\max}$ [b]	$\bar{X}$ [c]	$\tilde{X}$ [d]	$X_{25\%}$ [e]	$X_{75\%}$ [f]	σ_x [g]
$\langle |\boldsymbol{B}_o| \rangle_{\mathrm{up}}$ (nT)	1.04	17.4	5.96	5.59	3.99	7.10	3.01
$\langle n_i \rangle_{\mathrm{up}}$ (cm^{-3})	0.60	21.3	8.34	8.00	3.70	12.1	5.32
$\langle \beta_{\mathrm{tot}} \rangle_{\mathrm{up}}$ (N/A)	0.03	3.86	0.50	0.38	0.19	0.60	0.60
$\langle |V_{\mathrm{shn}}| \rangle_{\mathrm{up}}$ (km s^{-1})	155	699	460	456	383	535	123
$\langle |U_{\mathrm{shn}}| \rangle_{\mathrm{up}}$ (km s^{-1})	36.9	401	126	110	83.3	145	70.2
θ_{Bn} (deg)	17.1	88.6	56.8	54.6	42.7	73.3	19.5
$\langle M_{\mathrm{A}} \rangle_{\mathrm{up}}$ (N/A)	1.06	15.6	2.79	2.41	1.86	3.06	2.10
$\langle M_f \rangle_{\mathrm{up}}$ (N/A)	1.01	6.39	2.12	1.86	1.58	2.35	0.94
$\langle M_f \rangle_{\mathrm{up}} / M_{\mathrm{cr}}$ (N/A)	0.41	5.14	1.08	0.91	0.77	1.19	0.70
$\langle M_f \rangle_{\mathrm{up}} / M_{ww}$ (N/A)	0.06	2.49	0.36	0.18	0.11	0.32	0.51
$\langle M_f \rangle_{\mathrm{up}} / M_{\mathrm{gr}}$ (N/A)	0.04	1.91	0.28	0.14	0.09	0.25	0.39
$\langle M_f \rangle_{\mathrm{up}} / M_{\mathrm{nw}}$ (N/A)	0.04	1.76	0.26	0.13	0.08	0.23	0.36

Notes. For symbol definitions, see Appendix A.
[a] Minimum.
[b] Maximum.
[c] Mean.
[d] Median.
[e] Lower quartile.
[f] Upper quartile.
[g] Standard deviation.

consistently yielded lower reduced chi-squared values, $\tilde{\chi}_s^2$, the symmetric bi-self-similar function was used as the default core model function. In the downstream of strong (i.e., $\langle M_f \rangle_{\mathrm{up}} \gtrsim 2.5$) IP shocks it was found that the asymmetric bi-self-similar function produced the best results and so was the default core model function.[13] Note that of all the core VDFs fit to a symmetric bi-self-similar function, ~80.5% satisfied $2.0 \leqslant s_{ec} \leqslant 2.05$. That is, the majority of the distributions would be nearly indistinguishable from a bi-Maxwellian on visual inspection. The halo and beam/strahl were modeled with a bi-kappa model function for all VDFs examined since they always have a power-law tail and previous work found kappa model functions to be the best approximation (e.g., Maksimovic et al. 2005; Štverák et al. 2009).

For each IP shock, an iterative process was followed to correct for the spacecraft potential, ϕ_{sc} (details found in Appendix B), and define fit parameter initial guess values and constraints to yield stable solutions for the most VDFs (detailed steps found in Appendix C, and list of initial guess values and constraints found in Supplemental Material ASCII files (Wilson et al. 2019c) described in Appendix F). The process of defining the initial guess values and constraints is discussed in Section 3.2, and the quantified estimates of the fit quality are discussed in Section 3.3.

A total of 15,314 electron VDFs were observed by the *Wind* spacecraft within ±2 hr of 52 IP shocks. Of those 15,314 VDFs, 15,210 progressed to fit analysis, and stable model function parameters were found for 14,847 (~98%) core fits, 13,871 (~91%) halo fits, and 9567 (~63%) beam/strahl fits. The reason for the large disparity in beam/strahl fits compared

to the other two components will be discussed in Section 3.3 and Appendix C.

3.1. Velocity Distribution Functions

This section introduces and defines the model functions used to fit to the particle VDFs in this study with examples provided to illustrate shape and dependences on parameters.

The most common VDF used to model particle VDFs in space plasmas is the bi-Maxwellian (e.g., Feldman et al. 1979a, 1979b, 1983b; Kasper et al. 2006), given by

$$f(V_{\parallel}, V_{\perp}) = A_M \, e^{-\left[\left(\frac{V_{\parallel} - v_{o\parallel}}{V_{T\parallel}} \right)^2 + \left(\frac{V_{\perp} - v_{o\perp}}{V_{T\perp}} \right)^2 \right]}, \tag{1a}$$

where A_M is given by

$$A_M = \frac{n_o}{\pi^{3/2} V_{T\perp}^2 V_{T\parallel}}, \tag{1b}$$

where $v_{o,j}$ is the drift speed of the peak relative to zero along the jth component, $V_{T,j}^2$ is the thermal speed given by Equation (6c), V_j is the velocity ordinate of the jth component, and n_o is the number density.

The second most popular model VDF is the kappa distribution. The kappa velocity distribution has gained popularity in recent years owing to improvements in particle detectors and the ubiquitous non-Maxwellian tails observed for both ions and electrons (e.g., Mace & Sydora 2010; Pulupa et al. 2014b; Lazar et al. 2015a, 2015b, 2016, 2017, 2018; Livadiotis 2015; Livadiotis et al. 2018; Saeed et al. 2017; Shaaban et al. 2018), but references to and use of kappa or kappa-like (e.g., modified Lorentzian) distributions have been around for decades (e.g., Vasyliunas 1968; Feldman et al. 1983a; Maksimovic et al. 1997; Salem et al. 2003). It is beyond the scope of this study to explain the physical interpretation/ origin of this function, but there are several detailed discussions

---

[13] The parallel and perpendicular profiles at low energies differ greatly in these regions and required the use of the asymmetric function to accommodate the differences. Using a symmetric function resulted in very poor fit qualities, as defined in Section 3.3.
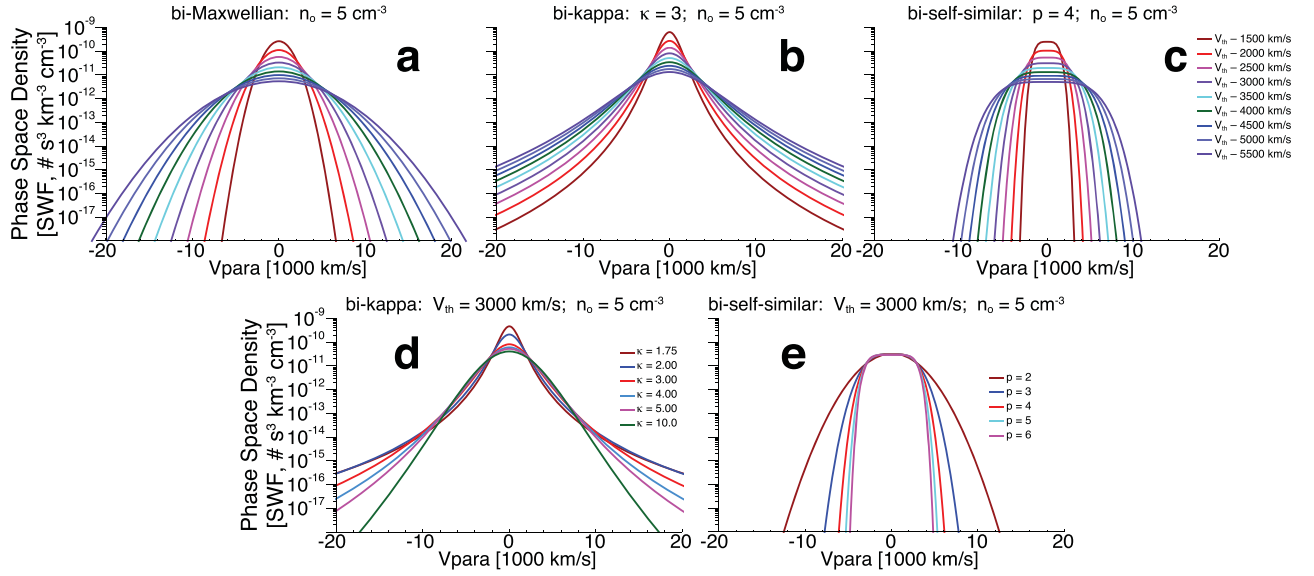
Figure 2. Examples of one-dimensional cuts through multiple model VDF functions to illustrate the functional dependence on various parameters. The top row (panels (a) through (c)) shows the dependence on the thermal speed, denoted generically as V_{th} here. The bottom row (panels (d) and (e)) shows the exponent dependencies. Panel (a) shows bi-Maxwellian VDFs (Equation 1(a)), panels (b) and (d) show bi-kappa VDFs (Equation 2(a)), and panels (c) and (e) show bi-self-similar VDFs (Equations 3(a) and 4(a)). All examples shown have the same number density of 5 cm^{-3}, denoted generically as n_o here.

already published on the topic (e.g., Livadiotis 2015; Livadiotis et al. 2018). A generalized power-law particle distribution is given by a bi-kappa VDF (e.g., Mace & Sydora 2010; Livadiotis 2015), for electrons here as

$$f(V_\perp, V_\parallel) = A_\kappa \left\{ 1 + \frac{B_\kappa}{\left(\kappa - \frac{3}{2}\right)} \right\}^{-(\kappa+1)}, \qquad (2a)$$

where A_κ is given by

$$A_\kappa = \left[\frac{1}{\pi\left(\kappa - \frac{3}{2}\right)} \right]^{3/2} \frac{n_o\, \Gamma(\kappa + 1)}{V_{T\perp}^2\, V_{T\parallel}\, \Gamma\left(\kappa - \frac{1}{2}\right)} \qquad (2b)$$

and B_κ is given by

$$B_\kappa = \left[\left(\frac{V_\parallel - v_{o\parallel}}{V_{T\parallel}} \right)^2 + \left(\frac{V_\perp - v_{o\perp}}{V_{T\perp}} \right)^2 \right], \qquad (2c)$$

where $\Gamma(z)$ is the Riemann gamma function of argument z and V_{Tj} is again the most probable speed of a 1D Gaussian for consistency, i.e., it does not depend on κ.

The last model VDF is called a *self-similar distribution*, which results when a VDF evolves under the action of inelastic scattering (e.g., Dum et al. 1974; Dum 1975; Horton et al. 1976; Horton & Choi 1979; Jain & Sharma 1979; Goldman 1984) or flows through disordered porous media (e.g., Matyka et al. 2016). The symmetric form is given by

$$f(V_\parallel, V_\perp) = A_{SS}\, e^{-\left[\left(\frac{V_\parallel - v_{o\parallel}}{V_{T\parallel}} \right)^s + \left(\frac{V_\perp - v_{o\perp}}{V_{T\perp}} \right)^s \right]}, \qquad (3a)$$

where A_{SS} is given by

$$A_{SS} = \left[2\Gamma\left(\frac{1 + s}{s} \right) \right]^{-3} \frac{n_o}{V_{T\perp}^2 V_{T\parallel}}. \qquad (3b)$$

Note that V_{Tj} is again the most probable speed of a 1D Gaussian for consistency, i.e., it does not depend on s. Further, one can see that Equation 3(a) reduces to Equation 1(a) in the limit where $s \to 2$. The function in Equation 3(a) will be referred to as the symmetric self-similar distribution function.

A slightly more general approach can be taken where the exponents are not uniform, which will be referred to as the asymmetric self-similar distribution function. The asymmetric functional form is given by

$$f(V_\parallel, V_\perp) = A_{AS}\, e^{-\left[\left(\frac{V_\parallel - v_{o\parallel}}{V_{T\parallel}} \right)^p + \left(\frac{V_\perp - v_{o\perp}}{V_{T\perp}} \right)^q \right]}, \qquad (4a)$$

where A_{AS} is given by

$$A_{AS} = \frac{n_o\, \Gamma^{-1}\left(\frac{1+p}{p} \right) \Gamma^{-2}\left(\frac{1+q}{q} \right)}{2^3\, V_{T\parallel}\, V_{T\perp}^2}. \qquad (4b)$$

Again, this will reduce to a bi-Maxwellian in the limit where $p \to 2$ and $q \to 2$. Note that in the event that the exponents s, p, or q are not even integers, the velocity ordinates, $(V_\parallel - v_{o\parallel})$ and $(V_\perp - v_{o\perp})$, will become absolute values to avoid complex roots and negative values of $f(V_\parallel, V_\perp)$. Example one-dimensional cuts of these three model VDFs can be found in Figure 2 for comparison.

The self-similar exponents are mostly a new variable, since most previous work modeled the core electrons as a bi-Maxwellian (e.g., Štverák et al. 2008, 2009; Bale et al. 2013; Pulupa et al. 2014b). There are a few studies that used one-dimensional self-similar functions to model a select few electron VDFs near collisionless shocks (e.g., Feldman et al. 1983a, 1983b), finding values consistent with those presented in Table 2. However, these studies did not define the normalization parameter in terms of the number density and thermal speeds (see, e.g., Equations 3(a) and 4(a)), but rather found a numerical value from empirical fits, i.e., the normalization parameter was not coupled to the physical parameters of

the fit function. At least one study in the solar wind did define the normalization constant, but they only considered a one-dimensional, isotropic distribution (e.g., Marsch & Livi 1985). Although several theoretical works predicted ranges of possible self-similar exponent values under various extrema scenarios (e.g., Dum et al. 1974; Dum 1975; Horton et al. 1976; Horton & Choi 1979; Jain & Sharma 1979; Goldman 1984), this is the first time the model has been used on a statistically significant set of VDFs.

The following is an illustrative example that shows how the signal-to-noise ratio of particle detectors strongly depends on the number density and thermal speed and that hot, tenuous plasmas are much more difficult to measure and accurately model. Examine the one-dimensional cuts shown in Figures 2 and 4. The toy models in Figure 2 are shown to illustrate the effect of thermal speed and exponents on the model fit function peaks and shapes. Notice that increasing the thermal speed of the Maxwellian from $V_{Te} = 1500$ to $5500 \, \mathrm{km \, s^{-1}}$ drops the peak phase-space density by nearly two orders of magnitude. The cut line also passes the $\pm 20,000 \, \mathrm{km \, s^{-1}}$ velocity boundary (i.e., roughly the upper energy bound of the EESA Low instrument) at a phase-space density roughly one order of magnitude higher than the colder examples. That is, the change in thermal speed reduced the dynamic range of observed phase-space densities by three orders of magnitude. Suppose that one examines a more extreme example with $n_e = 15 \, \mathrm{cm^{-3}}$ and $V_{Te} = 10,000 \, \mathrm{km \, s^{-1}}$. In this case, the difference between the peak and the lowest phase-space density within the $\pm 20,000 \, \mathrm{km \, s^{-1}}$ velocity boundary would only be a factor of ~ 55, i.e., slightly more than one order of magnitude.

For reference, the list of potential free parameters is as follows (see Appendix A for symbol definitions):

(a) *Core*
    (a) n_{ec}
    (b) $V_{Tec,j}$ or $T_{ec,j}$
    (c) $v_{oec,j}$
    (d) s_{ec}
    (e) p_{ec}
    (f) q_{ec}
    (g) κ_{ec}
(b) *Halo*
    (a) n_{eh}
    (b) $V_{Teh,j}$ or $T_{eh,j}$
    (c) $v_{oeh,j}$
    (d) κ_{eh}
(c) *Beam/Strahl*
    (a) n_{eb}
    (b) $V_{Teb,j}$ or $T_{eb,j}$
    (c) $v_{oeb,j}$
    (d) κ_{eb}.

For more details about derivation and normalization constants, see the Supplemental Material (Wilson et al. 2019c).

3.2. Fit Parameter Constraints

This section involves the discussion of the constraints/limits placed on fit parameters for each electron component and justifies them based on physically significant assumptions.

As an illustrative example, Figure 3 shows the densities of the protons, alpha-particles, and three electron components (blue squares) and the associated uncertainties (red error bars) for a subcritical, quasi-perpendicular IP shock (see, e.g.,

Wilson et al. 2019c, for shock parameters) observed by *Wind* on 1996 April 2 at 10:07:57.525 UTC. For this event, the plasma parameters are listed below in the form *Min–Max (Mean)[Median]*:

(a) *Upstream*
    (a) $|\mathbf{B}_o| \sim 0.53$–$3.14(1.96)[1.53]$ nT;
    (b) $n_p \sim 11.3$–$15.8(12.0)[11.9]$ cm^{-3};
    (c) $n_\alpha \sim 0.06$–$0.18(0.10)[0.11]$ cm^{-3};
    (d) $s_{ec} \sim 2.00$–$2.09(2.00)[2.00]$ N/A;
    (e) $\kappa_{eh} \sim 2.83$–$12.2(4.46)[4.40]$ N/A;
    (f) $\kappa_{eb} \sim 1.67$–$12.6(4.85)[5.10]$ N/A;
    (g) $n_{ec} \sim 10.7$–$13.0(11.7)[11.5]$ cm^{-3};
    (h) $n_{eh} \sim 0.06$–$1.44(0.69)[0.54]$ cm^{-3};
    (i) $n_{eb} \sim 0.02$–$0.17(0.09)[0.09]$ cm^{-3};
(b) *Downstream*
    (a) $|\mathbf{B}_o| \sim 3.45$–$5.99(4.85)[5.19]$ nT;
    (b) $n_p \sim 14.9$–$19.7(18.0)[18.1]$ cm^{-3};
    (c) $n_\alpha \sim 0.14$–$0.27(0.19)[0.19]$ cm^{-3};
    (d) $s_{ec} \sim 2.00$–$2.07(2.01)[2.01]$ N/A;
    (e) $\kappa_{eh} \sim 2.72$–$6.96(4.39)[4.29]$ N/A;
    (f) $\kappa_{eb} \sim 2.74$–$7.27(4.45)[4.50]$ N/A;
    (g) $n_{ec} \sim 13.6$–$18.4(16.7)[16.8]$ cm^{-3};
    (h) $n_{eh} \sim 0.02$–$2.53(0.56)[0.44]$ cm^{-3};
    (i) $n_{eb} \sim 0.01$–$0.29(0.12)[0.11]$ cm^{-3}.

Note that there are two time periods after 11:00 UTC where a few fit results satisfy $n_{eb}/n_{eh} \geqslant 1$. Figure 3 is illustrative of some of the error analysis employed in the present study and the fact that the beam/strahl fit more often fails than the core or halo as evidenced by the number of points. Below the details of how the fit parameters are constrained/limited are outlined with physical arguments.

First, the present study differs from some previous studies in that the fits are performed on the two-dimensional VDF rather than separate fits on one-dimensional cuts of the two-dimensional VDF (e.g., Maksimovic et al. 2005; Pulupa et al. 2014a, 2014b). One of the limitations of the latter approach is that the distribution function is not necessarily a separable function, which can introduce difficulty for the physical interpretation of the results. However, the latter approach has numerous advantages, including the stability of the solutions and ease with which the solutions are found with nonlinear least-squares software, i.e., it is generally easier to fit to a one-dimensional cut than a two-dimensional distribution.

The present study uses the former approach to avoid the difficulties introduced for nonseparable functions. For instance, when fitting to the parallel one-dimensional cut, the amplitude of the VDF is directly tied to the amplitude of the perpendicular cut. The amplitude of all standard model two-dimensional, gyrotropic VDFs is dependent on n_s, $V_{Ts,\parallel}^{-1}$, and $V_{Ts,\perp}^{-2}$. While it is computationally possible to fix the amplitude to the observed amplitude of the data for each cut and only vary the respective thermal speeds/temperatures and exponents, the inversion to find n_s can be problematic if care is not taken. For instance, the normalization constants differ for one-dimensional cuts from the two-dimensional gyrotropic VDF (see, e.g., Equation 1(a)). Although this approach involves fewer free parameters and should thus be easier to fit, it is much more restrictive in parameter space, i.e., n_s only varies indirectly through the variation of the thermal speeds/temperatures and exponents.

Given that fitting to a two-dimensional gyrotropic VDF has more free parameters and orders of magnitude more degrees of
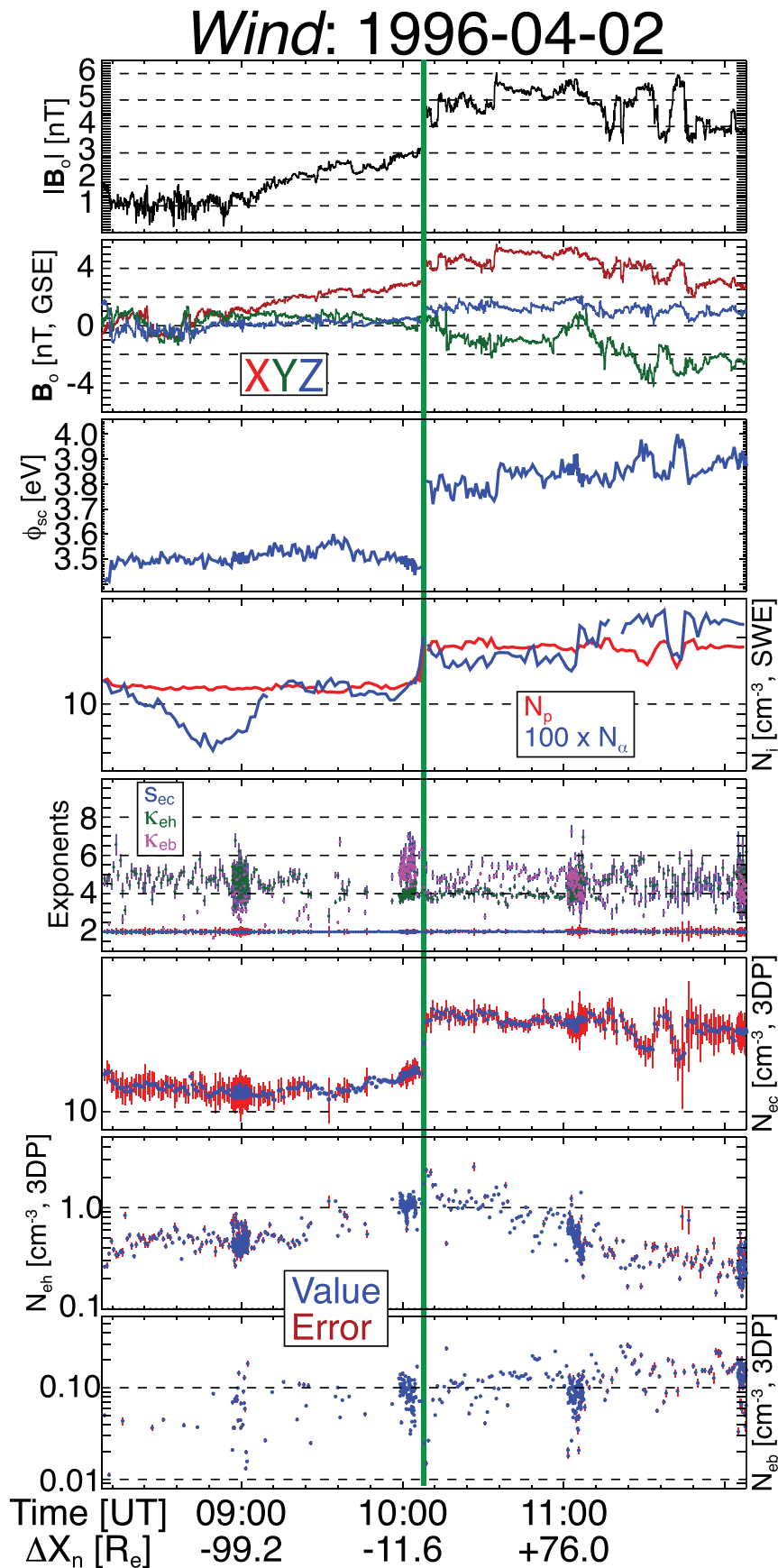
Figure 3. Example IP shock crossing observed on 1996 April 2 by the *Wind* spacecraft. The panels are as follows from top to bottom: $|\mathbf{B}_o|$ (nT), $\mathbf{B}_o$ (nT, GSE); value of spacecraft potential used for fits ϕ_{sc} (eV); n_p (red line) and $100 \times n_\alpha$ (blue line) (cm^{-3}, SWE); s_{ec} (blue circles), κ_{eh} (green circles), and κ_{eb} (magenta circles); n_{ec} values (blue circles) and uncertainty (red error bars) (cm^{-3}, 3DP fit); n_{eh} (cm^{-3}, 3DP fit); and n_{eb} (cm^{-3}, 3DP fit). The error bars for the four electron fit parameter panels are defined by the percent deviation discussed in Section 3.3. The error for this date satisfied $0.2\% < \delta\mathcal{R} \leqslant 54\%$ with a median of 10.3%.
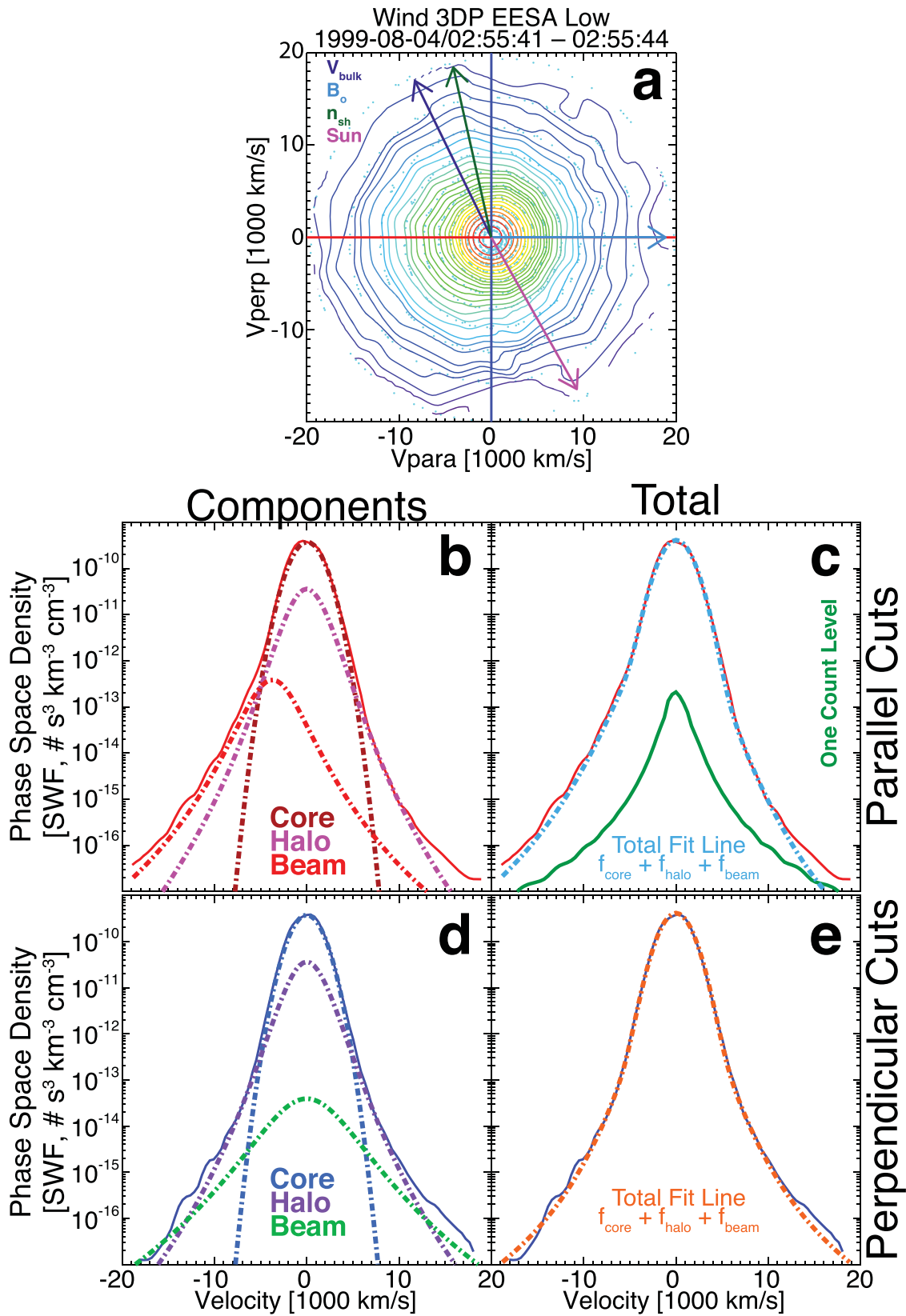
Figure 4. Example VDF observed at 02:55:41.008 UTC on 1999 August 4 by the *Wind*/3DP EESA Low detector. Panel (a) shows a 2D cut through the 3D VDF as contours of constant phase-space density, where the cut plane is defined by the unit vectors $(\boldsymbol{B}_o \times \boldsymbol{V}_i) \times \boldsymbol{B}_o$ on the vertical and $\boldsymbol{B}_o$ on the horizontal, where $\boldsymbol{B}_o = (+6.41, -7.64, -8.48)$ (nT, GSE). The origin in velocity space is defined by $\boldsymbol{V}_i = (-388.38, +3.13, -32.63)$ (km s^{-1}, GSE). The value of ϕ_{sc} for this VDF is 6.35 eV. Projected onto panel (a) are the following vectors: ion bulk flow velocity $\boldsymbol{V}_i$ or $\boldsymbol{V}_{bulk}$ (purple arrow), $\boldsymbol{B}_o$ (cyan arrow), shock normal vector $\boldsymbol{n}_{sh}$ (green arrow), and the Sun direction (magenta arrow). The small cyan circles show the location of actual measurements prior to regularized gridding with Delaunay triangulation. Panels (b) and (c) show the 1D parallel cuts along the horizontal (solid red line is data in both panels), and panels (d) and (e) show the 1D perpendicular cuts along the vertical (solid blue line is data in both panels). Panels (b) and (d) show the individual electron component fit results, while panels (c) and (e) show the sum of the fit results all as dashed lines and with color-coded labels. Panel (c) shows the one-count level for reference.

freedom, a stable solution requires reasonable constraints/limits on the variable parameters. There are some obvious boundaries determined by instrumental and physical constraints. As shown in the previous section, the difference between the highest and lowest phase-space densities is important for the signal-to-noise ratio, but it is also relevant to fitting model functions to the data. For instance, if an electron distribution had a population with $V_{Te} \gtrsim 10,000 \,\mathrm{km\,s^{-1}}$, the weights would not provide sufficient contrast between the peak and tails to constrain a stable and reliable fit without multiple imposed constraints. In contrast, electron VDFs with thermal speeds below $\sim 1000 \,\mathrm{km\,s^{-1}}$ fall below the lowest energy of the detector and so would be artificially hotter if they were observed (e.g., Paschmann & Daly 1998). A similar effect is often observed by spacecraft with electrostatic analyzers designed for the magnetosphere, not the comparatively cold, fast solar wind beam (e.g., McFadden et al. 2008a, 2008b; Pollock et al. 2016).

Statistical studies of the solar wind have shown that the maximum range of the total electron temperature is $T_{e,j} \sim 2.29$–$77.2 \,\mathrm{eV}$ or $V_{Te,j} \sim 450$–$2600 \,\mathrm{km\,s^{-1}}$ (e.g., Wilson et al. 2018). Previous studies have found that the electron halo temperatures satisfy $T_{e,j} \sim 14$–$560 \,\mathrm{eV}$ or $V_{Teh,j} \sim 1100$–$7000 \,\mathrm{km\,s^{-1}}$ (e.g., Feldman et al. 1975, 1978, 1979a; Maksimovic et al. 1997, 2005; Skoug et al. 2000; Tao et al. 2016a, 2016b; Lazar et al. 2017). Previous studies have also found that the electron beam/strahl temperatures satisfy $T_{eb,j} \sim 20$–$150 \,\mathrm{eV}$ or $V_{Te,j} \sim 1300$–$3600 \,\mathrm{km\,s^{-1}}$ (e.g., Ogilvie et al. 2000; Viñas et al. 2010; Tao et al. 2016a, 2016b). Thus, a range of allowed core thermal speeds from ~ 1000 to $\sim 10,000 \,\mathrm{km\,s^{-1}}$ can be assumed.

There are similar instrumental constraints on the drift speed of the three components. The core, however, is not likely to exhibit drift speeds (in the ion rest frame) in excess of several hundred kilometers per second (e.g., Pulupa et al. 2014a). In the present work, most fit results show less than $50 \,\mathrm{km\,s^{-1}}$, i.e., only 1838 of 14,847, or $\sim 12\%$, have drift speeds exceeding $50 \,\mathrm{km\,s^{-1}}$, consistent with previous work.[14] In contrast, owing to the physical interpretation of the strahl/beam component, most (8848 of 9567, or $\sim 92\%$) have drift speeds in excess of $1000 \,\mathrm{km\,s^{-1}}$. The allowed core, halo, and beam/strahl drift speeds loosely ranged from ~ 1000 to $\sim 10,000 \,\mathrm{km\,s^{-1}}$ for most events. In some events, a lower bound was imposed to prevent unphysical fit results, e.g., beam/strahl component with near zero drift speed (see Supplemental Material ASCII files (Wilson et al. 2019c) described in Appendix F for ranges for specific events). Note that $V_{oes,\perp}$ was fixed during the fitting, i.e., it was not allowed to vary. Originally this parameter was free to vary but resulted in fewer stable fits and rarely varied by more than a few kilometers per second. In some events, an explicit $V_{oec,\perp}$ was set as the initial guess values determined from examination of the distributions, but this is for a small minority of events (333 of 14,847, or $\sim 2\%$).

It has also been empirically found that the EESA Low detector has issues when $n_{ce} \lesssim 0.5 \,\mathrm{cm^{-3}}$ or $n_{ce} \gtrsim 50 \,\mathrm{cm^{-3}}$ for typical solar wind thermal speeds.[15] This is rarely an issue, as only 41 of the 14,847 VDFs analyzed (or $\sim 0.3\%$) have fit results falling outside the range ~ 0.5–$50 \,\mathrm{cm^{-3}}$. Note that the total electron density, $n_e = n_{ec} + n_{eh} + n_{eb} \sim n_e = n_p + 2n_\alpha$, is constrained by the total ion density from SWE and the total electron density from the upper hybrid line observed by the WAVES radio receiver (Bougeret et al. 1995), when possible (see Appendix B for more details).

Physically, the halo and beam/strahl components are suprathermal; thus, they should not have the dominant contribution to the total phase-space density of the VDF. Therefore, it is physically consistent to assume that the fit results should satisfy $n_{eh}/n_{ec} < 1$ and $n_{eb}/n_{ec} < 1$. The solutions were constrained to satisfy $n_{eh}/n_{ec} < 0.5$ and $n_{eb}/n_{ec} < 1$ based on results found in previous studies near 1 au (e.g., Feldman et al. 1975; Maksimovic et al. 1997, 2005; Skoug et al. 2000; Štverák et al. 2009; Viñas et al. 2010; Pierrard et al. 2016; Tao et al. 2016b).

In numerous previous studies that assumed a three-component solar wind electron VDF near 1 au (e.g., Maksimovic et al. 2005; Štverák et al. 2009; Pulupa et al. 2014a, 2014b), constraints were sometimes assumed such as that the fits satisfy $n_{eb}/n_{eh} < 1$. There is no restriction on this ratio[16] imposed during the fit process, and 1824 of 9313 (or $\sim 20\%$) of the fits satisfy $n_{eb}/n_{eh} \geqslant 1$. In fact, it was found that imposing the constraint $n_{eb}/n_{eh} < 1$ during the fit process actually greatly reduced the number of stable solutions found for the beam/strahl component.[17] Previous work did show that the ratio n_{eb}/n_{eh} decreases with increasing radial distance from the Sun, dropping below unity before 1 au, on average, but the ranges overlapped, allowing for $n_{eb}/n_{eh} \geqslant 1$ (e.g., Štverák et al. 2009).

Another constraint that is often assumed/used is that the strahl/beam component be only antisunward along $\boldsymbol{B}_o$ (e.g., Maksimovic et al. 2005; Štverák et al. 2009; Pulupa et al. 2014a, 2014b), though some magnetic field topologies have sunward-directed beam/strahl components (e.g., Owens et al. 2017). This constraint is imposed in this study, but it is important to note that some IP shocks examined have observable electron foreshocks. A consequence is that the halo component of the fit results effectively absorbs both the halo and the shock-reflected electron component in the events where this is directed sunward along $\boldsymbol{B}_o$ (this is very rare). If the shock-reflected electron component is directed antisunward, they will be included in the beam/strahl fit (this is much more common). The net result for the former is a smaller $(T_\perp/T_\parallel)_{eh}$ and on the latter is a larger $(T_\perp/T_\parallel)_{eb}$ and n_{eb}.

The lower bound of possible κ_{es} values is defined for mathematical/physical reasons as being $\gtrsim 3/2$ (e.g., Livadiotis 2015; Livadiotis et al. 2018). The upper bound is set to 100 solely because above that value the difference between a bi-Maxwellian and bi-kappa VDF is smaller than the accuracy of the measurements. Although the upper bound is allowed to extend to 100, the typical upper bound observed near 1 au is <20 (e.g., Maksimovic et al. 1997; Štverák et al. 2009; Pierrard et al. 2016; Tao et al. 2016a, 2016b; Lazar et al. 2017). The range of possible values for s_{ec}, p_{ec}, or q_{ec} falls between 2 and 10 for physical reasons (e.g., Dum et al. 1974; Dum 1975;

---

[14] Note that in the present work the dipole correction to ϕ_{sc} was not applied, which affects the drift velocity and heat flux velocity moments. Thus, the core drift velocities in our work suffer the greatest from this correction.

[15] Technically, this is an issue for nearly all electrostatic analyzers designed and flown to date. This is largely unavoidable without increasing the dynamic range of the detector significantly.

[16] The number of good ratios differs from the number of beam/strahl fits because some VDFs had a stable halo or beam/strahl but not the converse.

[17] Note that there was a post-fit constraint imposed limiting $n_{eb}/n_{eh} < 3$ because it was found empirically that most fits exceeding this threshold were bad/unphysical. However, not all were bad as evidenced by the example in Figure 6.

Horton et al. 1976; Horton & Choi 1979; Jain & Sharma 1979; Goldman 1984).

Finally, by definition the halo and beam/strahl components represent the lowest-energy suprathermal components of the electrons. Therefore, it is natural to assume that $T_{eh}/T_{ec} > 1$. There is no explicit restriction on this ratio imposed, and only 384 of 13,867 (or $\sim$3%) of the fits satisfy $T_{eh}/T_{ec} < 1$, and these occur downstream of strong shocks where core heating dominates. However, there are numerous events where limits/constraints were imposed on the component temperatures individually. So the low percentage is not entirely unexpected. In contrast, there were no corresponding attempts to limit T_{eh}/T_{eb} in any way other than to fit to the data.

3.3. Quality Analysis

The initial approach was to use the reduced chi-squared value $\tilde{\chi}_s^2$ of component s (see Appendix D for definition) as a test of the quality of the fit. However, it was quickly determined that some fit lines matched well with the data but had $\tilde{\chi}_s^2 > 10$ while others did not fit well at all despite having $\tilde{\chi}_s^2 \lesssim 1$. The issue is partly related to the calibration of the detector and thus the quality of the $\mathcal{W}$ values (see Appendix B for more details). The issue is also related to fitting a gyrotropic model function to data that is not, in general, gyrotropic. A possible improvement would fold the entire VDF into a forced gyrotropy prior to fitting to improve counting statistics and the comparison between data and model functions, but that is beyond the scope of the current study. Therefore, a new quantity was defined to provide an additional definition of the quality of any given fit by direct comparison.

Let us use $f^{(0)}$ as the actual data and $f^{(m)}$ $(=f^{(\text{core})} + f^{(\text{halo})} + f^{(\text{beam})})$ as the total model fit results. Then one can define the ratio of these two parameters as $\mathcal{R} = f^{(0)}/f^{(m)}$, which is a two-dimensional array of values. Then one calculates the median of this array, $\tilde{\mathcal{R}}$, to determine the percent deviation given by

$$\delta\mathcal{R} = |1 - \tilde{\mathcal{R}}| \cdot 100\%, \qquad (5)$$

where $\delta\mathcal{R}$ is computed for each electron VDF. The values of $\delta\mathcal{R}$ were then used as uncertainties/error bars for all fit parameters for the associated VDF for all components. In general, the percent magnitude of the uncertainty in each of the six fit parameters should not be uniform as is used herein (see Appendix E for discussion of 1σ uncertainties). The uncertainty of any variable calculated using these fit parameters was propagated assuming uncorrelated errors.

Note that the $\delta\mathcal{R}$ value alone does not always characterize the quality of any given fit. Therefore, a combination of parameters is chosen to define a set of fit quality flags from best with a value of 10 to worst with a value of 0 (see Appendix F for definitions). In general, fits with flags of at least 2 or higher can be used, but low fit flags should be treated with caution. Only $\lesssim$1% of all core, halo, and beam/strahl fits had flags of 1, while >95% of core, >89% of halo, and >61% of beam/strahl flags were at least 2.

Figure 4 shows an example VDF that had a low $\tilde{\chi}_s^2$ for each component and a $\delta\mathcal{R} \sim 3.0\%$, i.e., this is an example of an ideal fit. The distribution was fit using a symmetric bi-self-similar distribution for the core and a bi-kappa distribution for both the halo and beam/strahl components. The fit results are as follows:

1. $n_{e\{c,h,b\}} = \{15.43, 2.01, 0.056\}$ cm^{-3};
2. $V_{Te\{c,h,b\},\parallel} = \{1959.6, 2500.0, 3964.7\}$ km s^{-1};
3. $V_{Te\{c,h,b\},\perp} = \{1937.9, 2575.5, 4516.2\}$ km s^{-1};
4. $V_{oe\{c,h,b\},\parallel} = \{+44.58, -0.00, -3898.7\}$ km s^{-1};
5. $V_{oe\{c,h,b\},\perp} = \{-0.00, -0.00, -0.00\}$ km s^{-1};
6. $\{s_{ec}, \kappa_{eh}, \kappa_{eb}\} = \{2.00, 4.58, 2.57\}$, where s_{ec} is the self-similar exponent and κ_{es} is the kappa value;
7. $\tilde{\chi}_{e\{c,h,b\}}^2 = \{1.07, 1.36, 0.41\}$;
8. $\tilde{\chi}_{\text{tot}}^2 = 6.14$; and
9. Fit Flag {c,h,b} = {10, 10, 10}.

In contrast, Figure 5 shows an example VDF that had a high $\tilde{\chi}_s^2$ for two components yet still a small $\delta\mathcal{R} \sim 9.4\%$, i.e., this is still an example of a good fit despite the bad $\tilde{\chi}_s^2$ values for the core and beam/strahl fits. The fit results are as follows:

1. $n_{e\{c,h,b\}} = \{4.41, 0.57, 0.32\}$ cm^{-3};
2. $V_{Te\{c,h,b\},\parallel} = \{3882.6, 2624.5, 4574.5\}$ km s^{-1};
3. $V_{Te\{c,h,b\},\perp} = \{2728.2, 2986.3, 2387.6\}$ km s^{-1};
4. $V_{oe\{c,h,b\},\parallel} = \{-0.00, -594.9, +2000.0\}$ km s^{-1};
5. $V_{oe\{c,h,b\},\perp} = \{-0.00, -0.00, -0.00\}$ km s^{-1};
6. $\{p_{ec}, q_{ec}, \kappa_{eh}, \kappa_{eb}\} = \{4.00, 2.00, 2.27, 4.61\}$, where $p_{ec}(q_{ec})$ is the parallel (perpendicular) self-similar exponent and κ_{es} is the kappa value;
7. $\tilde{\chi}_{e\{c,h,b\}}^2 = \{28.5, 0.55, 14.4\}$;
8. $\tilde{\chi}_{\text{tot}}^2 = 14.40$; and
9. Fit Flag {c,h,b} = {4, 6, 5}.

Further, the example VDF in Figure 5 differs from that in Figure 4 in that an asymmetric self-similar model is used for the former. The total fit lines also illustrate a weakness of the method used. Since the components are fit separately, the respective weights change with each fit to prevent the fitting software from giving too much emphasis to, for instance, the core of the distribution when fitting to the halo.[18] Thus, the resultant $f^{(m)}$ can exceed $f^{(0)}$ in some places. The software does a post-fit check for instances where either the combined or any component model fit exceeds the data by user-specified factors.[19] For most events, the threshold is set between $\sim$2 and 4, but this varies, as some events have known issues. For instance, the known density from the upper hybrid line is 10 cm^{-3}, but no variation of ϕ_{sc} yields fit results with $n_e \sim 10$ cm^{-3} without the model exceeding the data at low energies. The reason is related to known calibration issues (see Appendix B).

Finally, Figure 6 shows an example VDF that had a high $\tilde{\chi}_s^2$ for the core component and moderate for beam/strahl but a small $\delta\mathcal{R} \sim 2.1\%$. This example VDF was chosen to illustrate a good fit even when $n_{eb}/n_{eh} > 1$. As previously discussed, there are post-fit constraints applied to the data based on statistical and physical constraints. The constraint relevant to Figure 6 is that requiring $n_{eb}/n_{eh} < 3$. This is why the fit flag value for the beam/strahl is zero and why $\tilde{\chi}_{\text{tot}}^2$ is larger than a few. The fit results are as follows:

1. $n_{e\{c,h,b\}} = \{3.37, 0.03, 0.14\}$ cm^{-3};
2. $V_{Te\{c,h,b\},\parallel} = \{2609.8, 5293.2, 4686.9\}$ km s^{-1};
3. $V_{Te\{c,h,b\},\perp} = \{2286.9, 5494.9, 2516.2\}$ km s^{-1};

---

[18] That is, the weights for the halo and beam/strahl fits are modified to force the software to examine only one side of the velocity distribution at a time. The weights also remove elements from the core fit to avoid including the core in the fit.
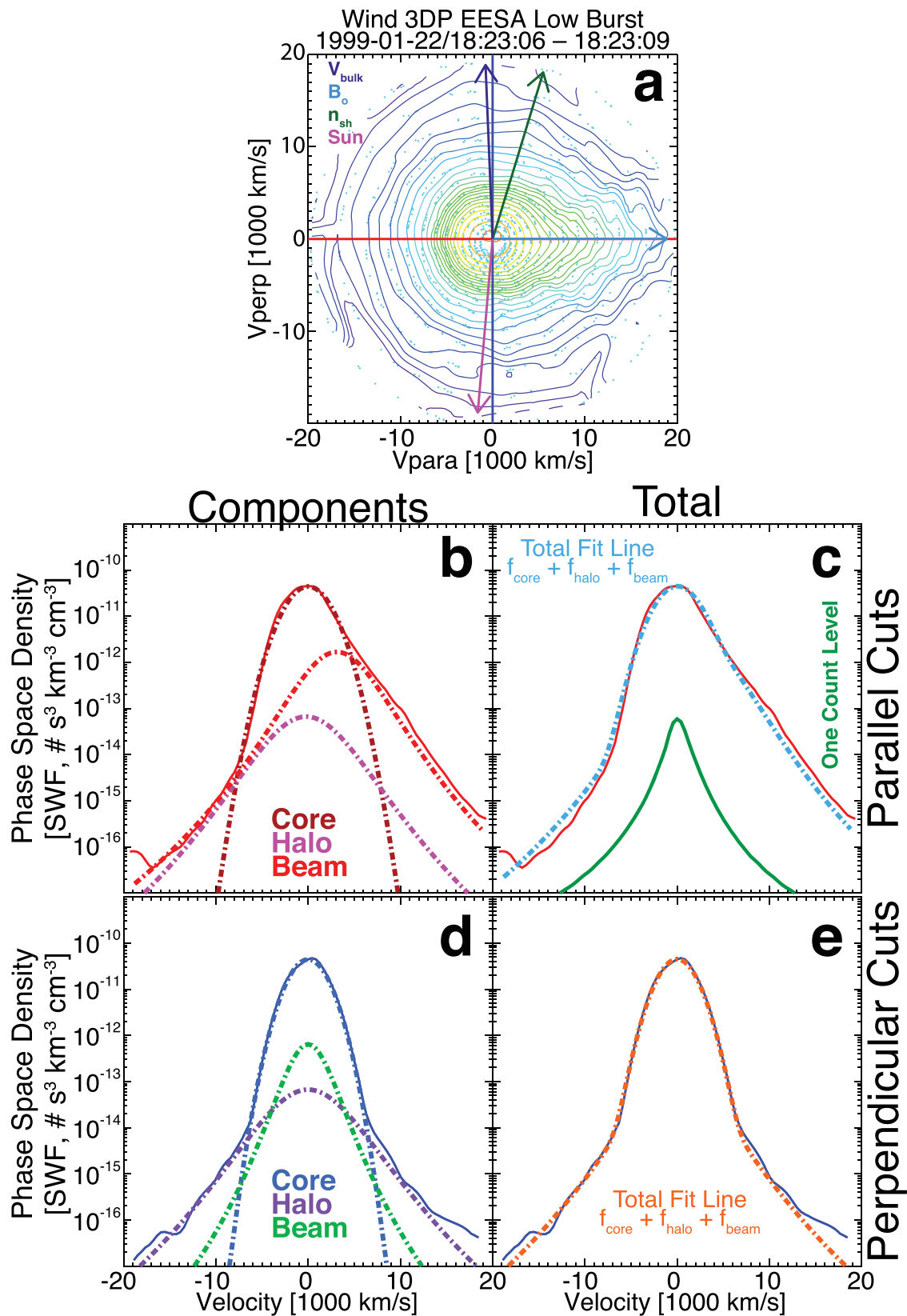
[19] For instance, below $\sim$1000 km s^{-1} in Figure 5 the magnitude of $f^{(m)}/f^{(0)}$ stays below $\sim$1.7 and exceeds 2.0 on the antiparallel side above $\sim$10,000 km s^{-1}. The latter was not flagged by the software because it resulted from the beam/strahl fit and that is the only fit to the parallel side for this VDF.
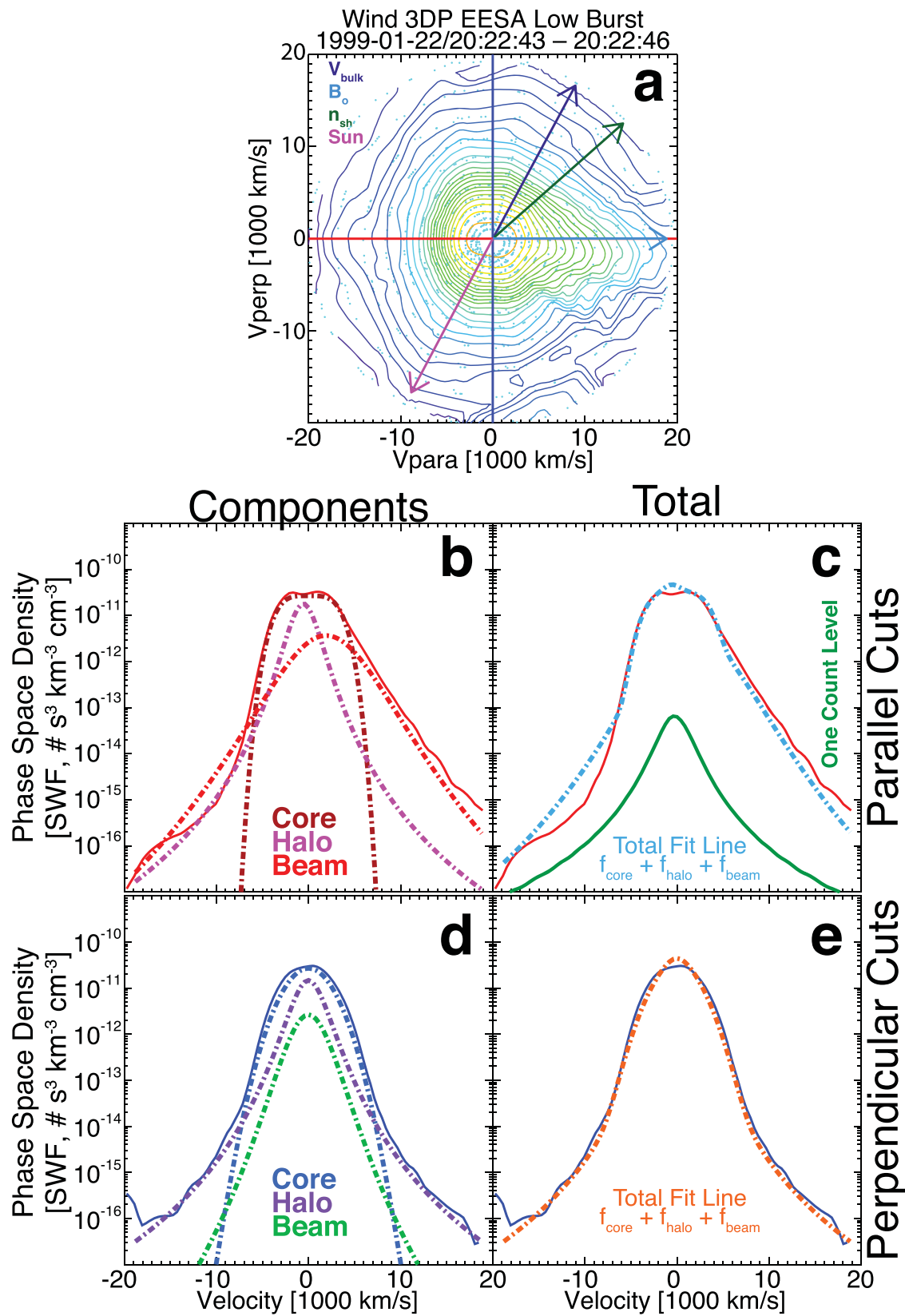
Figure 5. Another example VDF observed at 20:22:43.490 UTC on 1999 January 22 by the *Wind*/3DP EESA Low detector in burst mode. The format is the same as in Figure 4, where this VDF has $B_o = (-6.95, +9.78, -8.77)$ (nT, GSE), $V_i = (-619.12, +26.66, +21.19)$ (km s^{-1}, GSE), and $\phi_{sc} = 9.45$ eV.

4. $V_{oe\{c,h,b\},\parallel} = \{-0.00, -222.8, +3273.0\}$ km s^{-1};
5. $V_{oe\{c,h,b\},\perp} = \{-0.00, -0.00, -0.00\}$ km s^{-1};
6. $\{s_{ec}, \kappa_{eh}, \kappa_{eb}\} = \{2.00, 3.83, 3.53\}$;

7. $\tilde{\chi}^2_{e\{c,h,b\}} = \{17.84, 0.17, 5.14\}$;
8. $\tilde{\chi}^2_{tot} = 13.17$; and
9. Fit Flag $\{c, h, b\} = \{6, 6, 0\}$.

Figure 6. Another example VDF observed at 18:23:06.116 UTC on 1999 January 22 by the *Wind*/3DP EESA Low detector in burst mode. The format is the same as in Figures 4 and 5, where this VDF has $\boldsymbol{B}_o = (-0.89, -0.32, -10.57)$ (nT, GSE), $\boldsymbol{V}_i = (-626.59, +93.06, +76.13)$ (km s^{-1}, GSE), and $\phi_{sc} = 10.67$ eV.

One can see from the figure that the halo component is rather weak compared to the beam/strahl, which could be the result of an enhancement from the electron foreshock of this IP shock or the fast nature of the solar wind upstream of this IP shock. Regardless, the purpose of this example is to illustrate that stable and good fit solutions can be found that satisfy $n_{eb}/n_{eh} > 1$ even at 1 au.
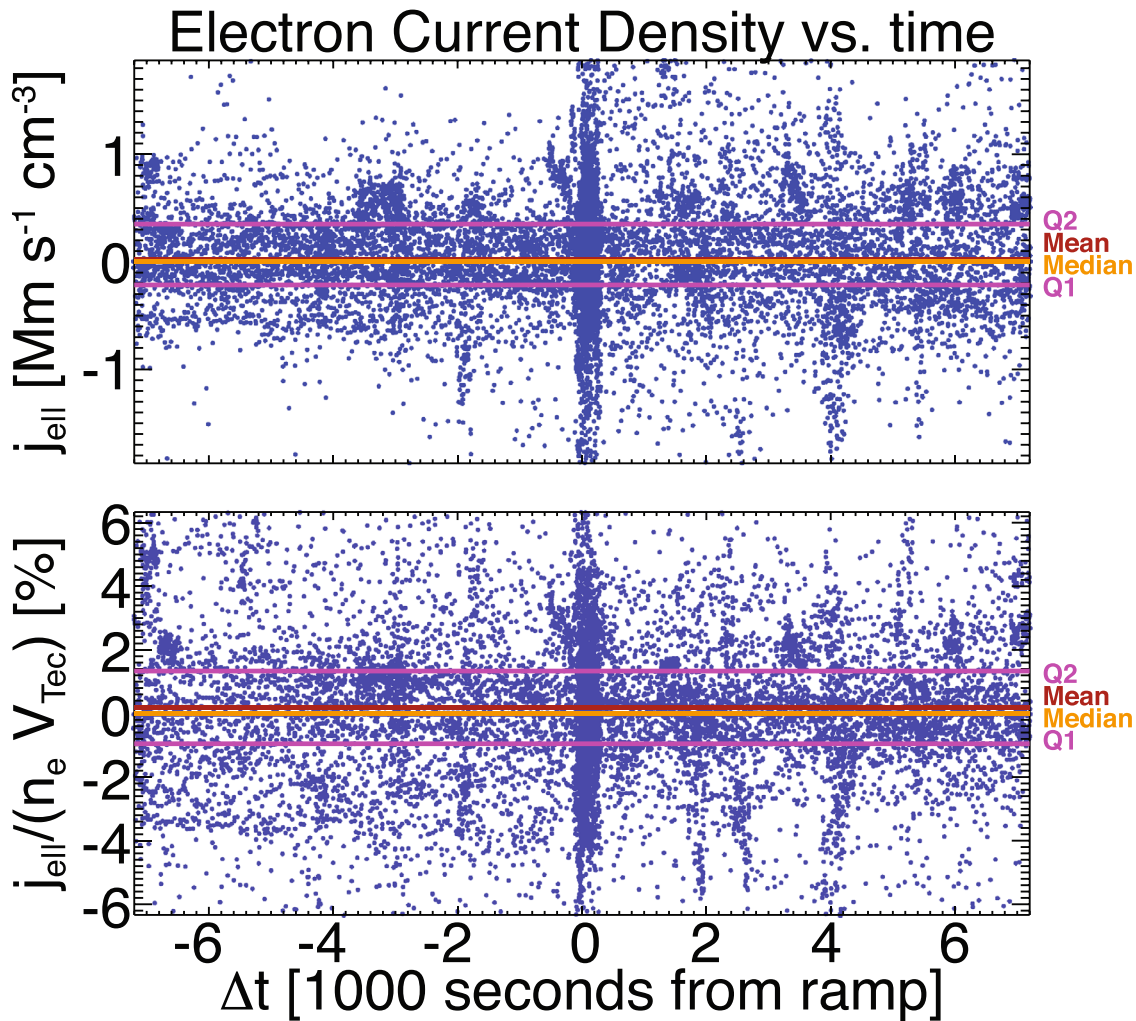
Figure 7. Two superposed epoch analysis plots of the total electron current density, $j_{e,\text{tot}}$ (Mm s^{-1}) (top panel), and normalized values, $j_{e,\text{tot}}/(n_e V_{Tec,\text{tot}})$ (%) (bottom panel), vs. seconds from the shock ramp center. Shown in each panel are the lower (Q1) and upper (Q2) quartiles as magenta lines, the mean as a red line, and the median as an orange line for all data. That is, the lines are computed for the entire set of data, not at each time stamp. For reference, the axis ranges were defined as 110% of the maximum of the absolute value of $X_{2.5}$ and $X_{97.5}$, where $X_{2.5}$ and $X_{97.5}$ are the bottom 2.5th and top 97.5th percentiles.

After examining thousands of fit results, it was determined that $\delta\mathcal{R}$ with $\tilde{\chi}_s^2$ and $\tilde{\chi}_{\text{tot}}^2$ are consistently more reliable quantities used in combination for defining the quality of the fit than using $\tilde{\chi}_s^2$ alone. The value is also used as a proxy for the uncertainty of any given fit parameter, e.g., $\delta n_{es} = \pm \, \delta\mathcal{R} \cdot n_{es}/2$ shown as the red error bars in Figure 3. Note that values of 100% correspond to fill values or bad fit results. In the following section the one-variable statistics of the $\tilde{\chi}_s^2$ and $\delta\mathcal{R}$ values are listed for reference to typical/expected values when evaluating the quality of a fit. In general, the best fits have small values for $\delta\mathcal{R}$ and all $\tilde{\chi}_s^2$.

Further tests of consistency were also performed to validate the fit results. First, the EESA Low detector is known to saturate when the count rate exceeds $\sim10^7$ counts s^{-1} (Lin et al. 1995). Examination of all VDFs found that a total of 10 energy-angle bins (from a total of 20,184,120), or $\sim5 \times 10^{-5}$%, exceeded the maximum count rate. Therefore, it is not thought that saturation has a significant impact on the methodology and results of this study. Second, as illustrated in Figure 3, the total electron density satisfies $n_e \sim n_p + 2n_\alpha$ for nearly all intervals. Statistically, the difference between the fit result for $n_e = n_{ec} + n_{eh} + n_{eb}$ and $n_p + 2n_\alpha$ is within expectations. The median, lower quartile, and upper quartile values are 10.3%, 4.9%, and 19.0%, respectively, which is consistent with our $\delta\mathcal{R}$ statistics.

Finally, the total electron current, $j_{e,\text{tot}} = \sum_s n_{es} \, v_{os,\|}$, in the ion rest frame should be zero to maintain a net zero current in the solar wind. The mean, median, lower quartile, and upper quartile for all data examined are ~22 km s^{-1} cm^{-3}, ~0 km s^{-1} cm^{-3}, ~-214 km s^{-1} cm^{-3}, and ~351 km s^{-1} cm^{-3}, consistent with previously published work on this data set (e.g., Bale et al. 2013; Pulupa et al. 2014a) and consistent with work in progress (C. S. Salem et al. 2019, in preparation). Normalizing $j_{e,\text{tot}}$ by n_e times $V_{Tec,\text{tot}}$ yields a mean, median, lower quartile, and upper quartile for all data examined of ~0.17%, $\sim10^{-8}$%, ~-0.95%, and ~1.3%, respectively. Thus, the values are all small compared to unity. Quantitatively, ~97.5% of the $j_{e,\text{tot}}/(n_e V_{Tec,\text{tot}})$ values satisfy $\lesssim5.5$%.

Figure 7 shows both $j_{e,\text{tot}}$ and $j_{e,\text{tot}}/(n_e V_{Tec,\text{tot}})$ versus seconds from every shock ramp center time in this study. One can see that although there are locations with significant deviation from zero (e.g., the shock ramp, which is not tremendously surprising, as that is where currents are supposed to exist), the mean (red horizontal line) and median (orange horizontal line) are small for both the raw and normalized current densities. Note that the data in Figure 7 include fit results where there may not be a solution for one or more components (see discussion of first data product ASCII file in Appendix F).

As a final note, there is the question about the validity of using a new model function to describe the thermal core. Of the 11,874 core VDFs fit with a symmetric bi-self-similar model function, there were 9559, or ~80.5%, that satisfied $2.0 \leqslant s_{ec} \leqslant 2.05$. That is, the majority of the distributions would be nearly indistinguishable from a bi-Maxwellian on visual inspection. Therefore, the use of the symmetric bi-self-similar model function is not entirely inconsistent with previous work that modeled the solar wind core with a bi-Maxwellian (e.g., Feldman et al. 1979a, 1979b). In fact, these results show that most core VDFs are not far from thermal velocity distributions, consistent with results showing evidence for collisional effects on the core (e.g., Salem et al. 2003; Bale et al. 2013).

3.4. Summary of Fit Results

For the 52 IP shocks examined there were a total of 15,314 VDFs observed by *Wind*. Of those 15,314 VDFs, 15,210 progressed to fit analysis, and for the core only 534 (~4%) were modeled as bi-kappa VDFs, 12,095 (~80%) were modeled as symmetric bi-self-similar VDFs, and 2581 (~17%) were modeled as asymmetric bi-self-similar VDFs. All core bi-kappa VDFs were found in the upstream, and all downstream core VDFs used either a symmetric or asymmetric bi-self-similar model. All halo and beam/strahl components were fit to a bi-kappa model. The justifications for the use of these functions are given in Section 3 and Appendix C. Of those 15,210 that progressed to fit analysis, stable solutions were found for 14,847 (~98%) $f^{(core)}$, 13,871 (~91%) $f^{(halo)}$, and 9567 (~63%) $f^{(beam)}$.

Recall that the fit results presented herein were performed on two-dimensional, (assumed) gyrotropic velocity distributions in the proton bulk flow rest frame. Most prior work numerically fit to one-dimensional cuts of the VDF or to one-dimensional reduced VDFs. There are benefits for either method, but here it is shown that the method employed is valid by illustrating the consistency with previous work. The statistical results of the densities are summarized below in the form *lower quartile–upper quartile(Mean)[Median]*:

(a) *All*
    (a) $n_{ec} \sim$ 6.44–19.5(13.7)[11.3] cm^{-3};
    (b) $n_{eh} \sim$ 0.21–0.63(0.52)[0.36] cm^{-3};
    (c) $n_{eb} \sim$ 0.09–0.27(0.21)[0.16] cm^{-3};
(b) *Upstream*
    (a) $n_{ec} \sim$ 4.06–12.5(8.90)[8.09] cm^{-3};
    (b) $n_{eh} \sim$ 0.17–0.49(0.42)[0.27] cm^{-3};
    (c) $n_{eb} \sim$ 0.09–0.26(0.22)[0.16] cm^{-3};
(c) *Downstream*
    (a) $n_{ec} \sim$ 8.44–24.2(17.3)[16.6] cm^{-3};
    (b) $n_{eh} \sim$ 0.26–0.70(0.59)[0.44] cm^{-3};
    (c) $n_{eb} \sim$ 0.09–0.28(0.21)[0.17] cm^{-3};

which are consistent with previous results near 1 au (e.g., Feldman et al. 1975, 1979a, 1983b; Maksimovic et al. 1997; Phillips et al. 1989a, 1989b; Nieves-Chinchilla & Viñas 2008; Skoug et al. 2000; Salem et al. 2001; Štverák et al. 2009; Pierrard et al. 2016). The full statistical results and associated histograms are presented in Paper II.

The statistical results of the quality analysis are listed below in the form *lower quartile–upper quartile(mean)[median]*:

(a) *All*
    (a) $\delta\mathcal{R} \sim$ 6.8%–16.3%(12.7%)[10.7%];
    (b) $\tilde{\chi}_c^2 \sim$ 0.90–4.28(6.47)[1.94];
    (c) $\tilde{\chi}_h^2 \sim$ 0.41–1.59(2.11)[0.72];
    (d) $\tilde{\chi}_b^2 \sim$ 0.36–1.28(1.50)[0.66];
    (e) $\tilde{\chi}_{tot}^2 \sim$ 2.85–9.39(1459)[4.92];
(b) *Upstream*
    (a) $\delta\mathcal{R} \sim$ 7.0%–16.1%(12.8%)[10.9%];
    (b) $\tilde{\chi}_c^2 \sim$ 0.74–3.66(3.99)[1.63];
    (c) $\tilde{\chi}_h^2 \sim$ 0.40–1.43(1.63)[0.66];
    (d) $\tilde{\chi}_b^2 \sim$ 0.31–0.98(0.93)[0.51];
    (e) $\tilde{\chi}_{tot}^2 \sim$ 2.69–8.47(1105)[4.50];
(c) *Downstream*
    (a) $\delta\mathcal{R} \sim$ 6.5%–16.4%(12.6%)[10.5%];
    (b) $\tilde{\chi}_c^2 \sim$ 1.10–6.32(9.12)[2.29];
    (c) $\tilde{\chi}_h^2 \sim$ 0.43–1.74(2.63)[0.78];
    (d) $\tilde{\chi}_b^2 \sim$ 0.47–1.72(2.14)[0.86];
    (e) $\tilde{\chi}_{tot}^2 \sim$ 3.03–10.7(1835)[5.43].

The purpose of listing these statistics is to provide a range of typical or expected $\tilde{\chi}_s^2$ and $\delta\mathcal{R}$ values for reference when determining the quality of any given fit. Note that the statistics for $\delta\mathcal{R}$ shown above were performed on arrays that excluded the lower and upper boundaries, i.e., 0.1% and 100% values. The statistical results of the model function exponent and drift speed results are presented below, and the full data product resulting from this work is described in Appendix F.

4. Exponents and Drifts

Table 2 shows the one-variable statistics for the exponents from the model fits of the electron VDFs for the core ($s = c$), halo ($s = h$), and beam/strahl ($s = b$). The VDFs, modeled as bi-kappa (κ_{es}), symmetric bi-self-similar (s_{es}), and asymmetric bi-self-similar velocity distributions (p_{es} for parallel and q_{es} for perpendicular), are summarized for all time periods, upstream only, downstream only, low Mach number only, high Mach number only, quasi-perpendicular only, and quasi-parallel only. The rows showing N/A (not available) for every entry had no fit results, i.e., the core was only modeled as a bi-kappa in the upstream and an asymmetric bi-self-similar only in the downstream, and therefore the converse had no results to examine.

For the VDFs fit to a bi-kappa, the core values typically lie between ~5 and 10, while the halo and beam/strahl lie in the ranges of ~3.5–5.4 and ~3.4–5.2, respectively. Only the core was fit to the bi-self-similar functions, and nearly all symmetric exponents are between ~2.00 and 2.04, while most of the asymmetric parallel and perpendicular exponents lie in the ranges of ~2.2–4.0 and ~2.0–2.5, respectively.

The κ_{eh} and κ_{eb} values are consistent with previous solar wind observations near 1 au (e.g., Maksimovic et al. 1997, 2005; Štverák et al. 2009; Pierrard et al. 2016; Tao et al. 2016a, 2016b; Lazar et al. 2017; Horaites et al. 2018). The κ_{ec} values are also consistent with previous solar wind observations (e.g., Nieves-Chinchilla & Viñas 2008; Broiles et al. 2016).

There are several interesting things to note from Table 2. The mean, median, and lower/upper quartile values for κ_{ec} are slightly higher for high than for low Mach number shocks, though only the median and lower quartile values are significant. Since a bi-kappa model was only used for upstream core VDFs, this may imply that shock strength is somehow dependent on the upstream core electron distribution profiles. One possible physical interpretation would be that the sound

Table 2
Electron Exponent Parameters

Exponent	$X_{\min}$ [a]	$X_{\max}$ [b]	$\bar{X}$ [c]	$\tilde{X}$ [d]	$X_{25\%}$ [e]	$X_{75\%}$ [f]
			All: 15,210 VDFs			
κ_{ec}	2.14	100.0	9.15	7.92	5.40	10.2
s_{ec}	2.00	3.00	2.03	2.00	2.00	2.04
p_{ec}	2.00	5.43	3.09	3.00	2.20	4.00
q_{ec}	2.00	3.29	2.24	2.00	2.00	2.46
κ_{eh}	1.51	19.7	4.62	4.38	3.58	5.34
κ_{eb}	1.52	20.0	4.57	4.17	3.40	5.16
			Upstream Only: 6546 VDFs			
κ_{ec}	2.14	100.0	9.15	7.92	5.40	10.2
s_{ec}	2.00	2.31	2.01	2.00	2.00	2.03
p_{ec}	N/A	N/A	N/A	N/A	N/A	N/A
q_{ec}	N/A	N/A	N/A	N/A	N/A	N/A
κ_{eh}	1.52	18.4	4.16	4.10	3.25	4.83
κ_{eb}	1.52	19.6	4.22	3.81	3.25	4.70
			Downstream Only: 8664 VDFs			
κ_{ec}	N/A	N/A	N/A	N/A	N/A	N/A
s_{ec}	2.00	3.00	2.05	2.01	2.00	2.06
p_{ec}	2.00	5.43	3.09	3.00	2.20	4.00
q_{ec}	2.00	3.29	2.24	2.00	2.00	2.46
κ_{eh}	1.51	19.7	4.94	4.62	3.80	5.70
κ_{eb}	1.53	20.0	4.82	4.45	3.61	5.44
			$\langle M_f \rangle_{\rm up} < 3$ Only: 12,988 VDFs			
κ_{ec}	2.14	100.0	9.02	6.83	4.40	9.93
s_{ec}	2.00	3.00	2.03	2.00	2.00	2.04
p_{ec}	2.00	5.43	3.10	3.00	2.18	4.00
q_{ec}	2.00	3.14	2.26	2.01	2.00	2.49
κ_{eh}	1.51	19.7	4.54	4.34	3.58	5.26
κ_{eb}	1.52	20.0	4.62	4.20	3.46	5.19
			$\langle M_f \rangle_{\rm up} \geqslant 3$ Only: 2222 VDFs			
κ_{ec}	4.32	27.2	9.30	8.60	6.89	10.4
s_{ec}	2.00	2.30	2.03	2.00	2.00	2.08
p_{ec}	2.00	5.00	3.08	2.50	2.18	4.00
q_{ec}	2.00	3.29	2.16	2.00	2.00	2.50
κ_{eh}	1.60	19.2	5.06	4.68	3.62	6.05
κ_{eb}	1.52	18.8	4.25	3.84	2.89	4.94
			$\theta_{Bn} > 45°$ Only: 10,940 VDFs			
κ_{ec}	4.05	27.2	7.77	7.18	4.84	9.11
s_{ec}	2.00	2.31	2.02	2.00	2.00	2.05
p_{ec}	2.00	5.43	3.00	2.62	2.17	4.00
q_{ec}	2.00	3.29	2.28	2.04	2.00	2.56
κ_{eh}	1.51	19.7	4.73	4.44	3.67	5.47
κ_{eb}	1.52	20.0	4.67	4.20	3.33	5.33
			$\theta_{Bn} \leqslant 45°$ Only: 4270 VDFs			
κ_{ec}	2.14	100.0	16.0	11.7	10.0	14.5
s_{ec}	2.00	3.00	2.06	2.00	2.00	2.04
p_{ec}	2.00	4.28	3.29	4.00	4.00	4.28
q_{ec}	2.00	3.00	2.14	2.00	2.00	2.16
κ_{eh}	1.55	19.4	4.32	4.18	3.37	5.09
κ_{eb}	1.53	16.5	4.31	4.10	3.57	4.82

Notes. For symbol definitions, see Appendix A.
[a] Minimum.
[b] Maximum.
[c] Mean.
[d] Median.
[e] Lower quartile.
[f] Upper quartile.

speed depends on the polytropic index for each species, i.e., the equation of state assumed for the system. A bi-kappa core VDF could affect the estimate of the sound speed, thus altering the

fast mode Mach number. However, the shape of the upstream VDFs will also affect the shock dissipation mechanisms. For instance, it is known that the existence of power-law tails improves the efficiency of shock acceleration (e.g., Trotta & Burgess 2019). Therefore, the larger κ_{ec} associated with higher Mach number shocks may imply that lower energy particles have entered the tails, thus increasing the exponent.[20]

In contrast, the asymmetric bi-self-similar exponents, only used in downstream regions, are effectively the same between low and high Mach number shocks. However, this changes when comparing quasi-parallel and quasi-perpendicular shocks. The p_{ec} exponent has higher mean, median, and lower/upper quartile values for quasi-parallel than quasi-perpendicular shocks. The opposite is true for the q_{ec} exponent.

This is interesting, as higher p_{ec} values are predicted to occur in the nonlinear saturation stages of ion-acoustic waves (e.g., Dum et al. 1974; Dum 1975). Such waves are driven by relative electron–ion drifts (i.e., currents) and are observed near both quasi-parallel and quasi-perpendicular shocks (e.g., Fuselier & Gurnett 1984; Wilson et al. 2007, 2010, 2012, 2014a, 2014b; Breneman et al. 2013), but their amplitudes increase with increasing shock strength (e.g., Wilson et al. 2007). If the largest ion-acoustic waves generate the largest values of p_{ec}, then one would expect maximum values downstream of strong quasi-perpendicular shocks, which is not the case here. This leads to the question of what fraction of energy goes to increasing p_{ec} versus what fraction goes to increasing $T_{ec,\parallel}$. This would depend on the effective inelasticity of the wave–particle interactions, where larger inelasticity increases p_{ec} and smaller inelasticity increases $T_{ec,\parallel}$ (e.g., Dum et al. 1974; Dum 1975; Horton et al. 1976; Horton & Choi 1979; Jain & Sharma 1979; Goldman 1984). The interaction between a wave and a particle can be treated as inelastic if the particle affects the wave amplitude and kinetic energy during the interaction. Most test-particle treatments do not handle this self-consistently, and if the effect is distributed to an entire VDF, the net result can be a stochastic heating that increases p_{ec} from 2.0 (e.g., Dum et al. 1974; Dum 1975).

Another theory predicts that flat-top electron distributions (i.e., $p_{ec} \rightarrow \geqslant 4$ and $q_{ec} \rightarrow \sim 2$–$3$) can result from the combined effects of a quasi-static, cross-shock electric potential and from fluctuation electric fields (e.g., Feldman et al. 1983a; Hull et al. 1998) through a process called maximal filling (e.g., Morse 1965). However, similar to the predictions for wave-driven flat tops, this theory should generate stronger flat tops (i.e., larger values of p_{ec}) for stronger quasi-perpendicular shocks, which we do not observe. Thus, the evolution of the electron VDFs does not seem consistent with the standard quasi-static, cross-shock electric potential, but rather in agreement with recent high-resolution observations at the bow shock (e.g., Chen et al. 2018; Goodrich et al. 2018).

Another interesting result is the difference in the κ_{eh} values under different conditions. When the values of κ_{eh} are larger (smaller), that implies a less (more) energized halo, i.e., softer (harder) spectra. One can see that κ_{eh} is larger downstream than upstream and near high rather than low Mach number shocks. That is, the halo is less energized downstream of IP shocks and near strong IP shocks than the converse, which is somewhat unexpected, as strong shocks should more readily energize suprathermal particles (e.g., Malkov & Drury 2001;

---

[20] Recall that κ_{ec} values only exist for upstream VDF fits, so the dependence on Mach number is not about thermalization.
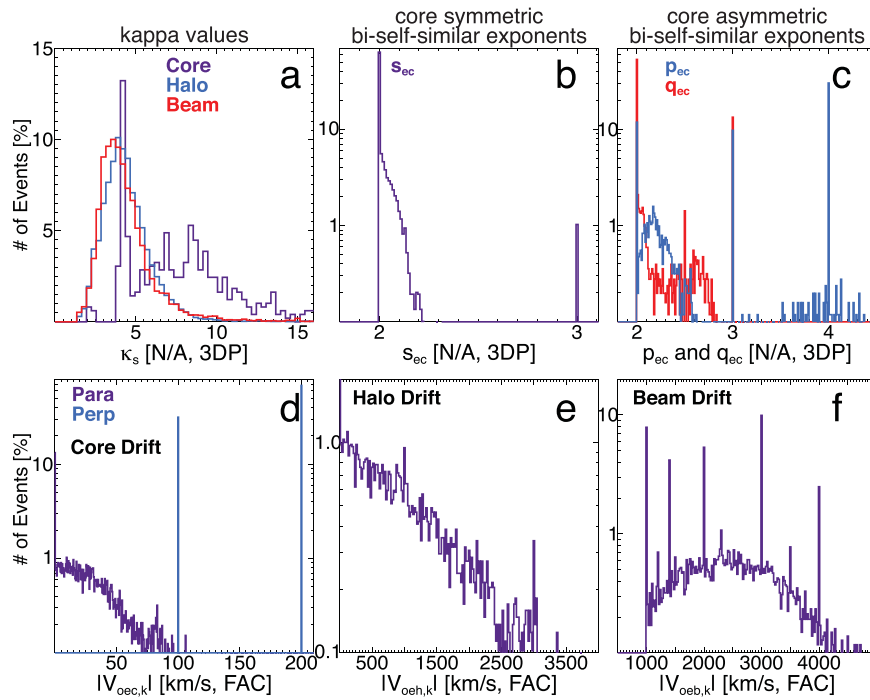
Figure 8. Histograms of the exponents (top row) and bulk drift velocity magnitudes (bottom row) for the different electron components for all time periods as percentage of total counts. Panel (a) shows the κ_{es} values for the core (violet), halo (blue), and beam/strahl (red) components. Panel (b) shows the s_{ec} for the core (violet). Panel (c) shows the p_{ec} (blue) and q_{ec} (red) values for the core. Panels (d)–(f) show the magnitude of the parallel (violet) and perpendicular (blue) drift velocities for the core, halo, and beam/strahl components, respectively. The statistics for the exponents are listed in Table 2. Note that the tick marks are individually labeled in all panels.

Treumann 2009; Caprioli & Spitkovsky 2014; Park et al. 2015; Trotta & Burgess 2019). In contrast, κ_{eh} is slightly smaller ($\sim$10%) near quasi-parallel than quasi-perpendicular shocks, which implies more energized halo electrons. Although quasi-parallel shocks are predicted (e.g., Malkov & Drury 2001; Caprioli & Spitkovsky 2014) and observed (e.g., Wilson et al. 2016) to be more efficient particle accelerators, the predictions are usually specific to ions, while mildly suprathermal electrons are thought to most efficiently interact with quasi-perpendicular shocks (e.g., Wu 1984; Park et al. 2013; Trotta & Burgess 2019). Further, very recent simulation results suggest that the upstream electron suprathermal tail will become flatter (i.e., smaller kappa values) with increasing Mach number for quasi-perpendicular shocks (Trotta & Burgess 2019). This may explain why both κ_{eh} and κ_{eb} are smaller in the upstream than downstream. The time evolution of these kappa values will be examined in more detail in Paper III.

A major caveat of the above discussion is the exchange of particles between the various electron VDF components, i.e., former core electrons can be energized and move to the halo or the converse. Therefore, one needs to be careful when interpreting the change in a given component-specific parameter. This will be discussed in more detail in Paper III.

Finally, the κ_{eb} values show a similar behavior between upstream and downstream and shock geometry as κ_{eh}, but they differ between low and high Mach number shocks. That is, stronger shocks appear to energize the beam/strahl component more than weaker shocks. This is likely due to the electron foreshock component observed upstream of strong IP shocks (e.g., Bale et al. 1999; Pulupa & Bale 2008; Pulupa et al. 2010), combined with the usual solar wind beam/strahl component.

Figure 8 shows histograms of κ_{es}, s_{ec}, p_{ec}, q_{ec}, and the drift speed magnitudes, $V_{oes,j}$ (s for electron components and j for

parallel or perpendicular), for the three electron populations. These histograms show distributions corresponding to the first part of Table 2, i.e., all VDF solutions. In many of the panels there are isolated, dominant peaks, nearly all of which result from constraints imposed for specific events, not necessarily an underlying physical reason. For instance, the peaks for $p_{ec} = 3$ and 4 in panel (c) are for strong shocks exhibiting flat-top VDFs in the downstream, where the fit routines were not finding stable solutions without imposing constraints on both the exponents and the minimum number density for the core distribution.

One can see that, as discussed previously, the core parallel drift speeds (violet line, panel (d)) tend to fall below $\sim$100 km s^{-1}, consistent with previous results (e.g., Pulupa et al. 2014a). In fact, most of the core and halo drifts are near zero, with the number of results satisfying $V_{oec,\parallel} \leqslant 1$ km s^{-1} and $V_{oeh,\parallel} \leqslant 1$ km s^{-1} being 8735 ($\sim$59%) and 7311 ($\sim$53%), respectively. Note that although there is sometimes a sizable perpendicular core drift (blue line, panel (d)) for some shock crossings, these were explicitly set after visual inspection of the VDFs during the iterative fitting process. The nonzero perpendicular drifts almost certainly result from inaccuracies in the calculation of the solar wind rest frame and a dipole correction to ϕ_{sc} not included in the present analysis (e.g., Pulupa et al. 2014a; see Appendix B for more details).

The magnitudes of $V_{oeh,\perp}$ and $V_{oeb,\perp}$ never deviated from zero.[21] The magnitudes of $V_{oeh,\parallel}$ range from $\sim$0 to 8860 km s^{-1}, with a lower to upper quartile range of

---

[21] This was an explicit constraint imposed on all fits but would also have resulted largely from the initial guess that both $V_{oeb,\perp}$ and $V_{oeb,\perp}$ equal zero. That is, the fit software uses initial guesses to estimate gradient magnitudes for changes between iterations. So if the initial guess is null, the step size will be null as well.

$\sim$0–850 km s^{-1} and a mean (median) of $\sim$580 km s^{-1} ($\sim$0.1 km s^{-1}). The magnitudes of $V_{oeb,\parallel}$ range from $\sim$1000 to 9330 km s^{-1}, with a lower to upper quartile range of $\sim$1750–3090 km s^{-1} and a mean (median) of $\sim$2580 km s^{-1} ($\sim$2480 km s^{-1}). As previously discussed, the lower bound for $V_{oeb,\parallel}$ was imposed on the basis of physical arguments, while the magnitude of $V_{oeh,\parallel}$ was allowed to go to zero. If only magnitudes satisfying $V_{oes,\parallel} > 1$ km s^{-1} are considered, the mean (median) and lower to upper quartile ranges are $\sim$42 km s^{-1} ($\sim$30 km s^{-1}) and $\sim$14–52 km s^{-1} for $V_{oec,\parallel}$ and $\sim$1227 km s^{-1} ($\sim$903 km s^{-1}) and $\sim$362–1695 km s^{-1} for $V_{oeh,\parallel}$.

5. Discussion

A total of 15,314 electron VDFs were observed by the *Wind* spacecraft within $\pm$2 hr of 52 IP shocks, of which 15,210 had a stable solution for at least one component. Stable model function parameters were found for 14,847 ($\sim$98%) core fits, 13,871 ($\sim$91%) halo fits, and 9567 ($\sim$63%) beam/strahl fits. The fit parameters are consistent with previous studies and will be discussed in detail in the following two parts of this study. Of the 15,210 VDFs examined herein, the core was modeled as a bi-kappa for 534 ($\sim$4%) VDFs, as a symmetric bi-self-similar for 12,095 ($\sim$80%) VDFs, and as an asymmetric bi-self-similar for 2581 ($\sim$17%) VDFs. This is the first statistical study to find that the core electron distribution is better fit to a self-similar VDF than a Maxwellian under all conditions.

The exponents are summarized below in the form *lower quartile–upper quartile*(*Mean*)[*Median*]:

(a) *All*
    (a) $s_{ec} \sim$ 2.00–2.04(2.03)[2.00];
    (b) $p_{ec} \sim$ 2.20–4.00(3.09)[3.00];
    (c) $q_{ec} \sim$ 2.00–2.46(2.24)[2.00];
    (d) $\kappa_{ec} \sim$ 5.40–10.2(9.15)[7.92];
    (e) $\kappa_{eh} \sim$ 3.58–5.34(4.62)[4.38];
    (f) $\kappa_{eb} \sim$ 3.40–5.16(4.57)[4.17];
(b) *Upstream*
    (a) $s_{ec} \sim$ 2.00–2.03(2.01)[2.00];
    (b) $p_{ec} \sim$ N/A;
    (c) $q_{ec} \sim$ N/A;
    (d) $\kappa_{ec} \sim$ 5.40–10.2(9.15)[7.92];
    (e) $\kappa_{eh} \sim$ 3.25–4.83(4.16)[4.10];
    (f) $\kappa_{eb} \sim$ 3.25–4.70(4.22)[3.81];
(c) *Downstream*
    (a) $s_{ec} \sim$ 2.00–2.06(2.05)[2.01];
    (b) $p_{ec} \sim$ 2.20–4.00(3.09)[3.00];
    (c) $q_{ec} \sim$ 2.00–2.46(2.24)[2.00];
    (d) $\kappa_{ec} \sim$ N/A;
    (e) $\kappa_{eh} \sim$ 3.80–5.70(4.94)[4.62];
    (f) $\kappa_{eb} \sim$ 3.61–5.44(4.82)[4.45].

Overall the κ_{eh} and κ_{eb} values are consistent with previous solar wind observations near 1 au (e.g., Štverák et al. 2009; Pierrard et al. 2016; Lazar et al. 2017; Horaites et al. 2018). The κ_{ec} values are also consistent with previous solar wind observations (e.g., Nieves-Chinchilla & Viñas 2008; Broiles et al. 2016). The values for s_{ec}, p_{ec}, and q_{ec} are consistent with previous results as well (e.g., Feldman et al. 1983a, 1983b).

The interesting aspect of VDFs being well modeled by bi-self-similar functions is that such functions are used to describe the evolution of distributions for either the flow through disordered porous media (e.g., Matyka et al. 2016) or the influence of inelastic scattering (e.g., Dum et al. 1974;

Dum 1975; Horton et al. 1976; Horton & Choi 1979; Jain & Sharma 1979; Goldman 1984). It is unlikely that the former applies directly, but the latter may be interpreted in the following manner. The typical approach for test-particle simulations used to examine wave–particle interactions does not include feedback from the particles on the waves. In a real plasma, the particles can alter three properties of electromagnetic waves: their amplitude (potential energy), momentum, and kinetic energy. Consider a simple scenario whereby a particle reflects off of an electromagnetic wave field along one dimension. If done self-consistently, the particle can reduce the wave amplitude in addition to affecting the field momentum and kinetic energy. In the case of a reduced wave amplitude, the resulting scattering problem can be treated as a simple inelastic collision.[22] Thus, the net result of an ensemble of particles interacting with a wave field can be stochastic (e.g., Dum et al. 1974; Dum 1975), which provides one physical justification for the use of the bi-self-similar functions. These functions are also convenient in that they reduce to bi-Maxwellians in the limit where the exponents go to 2, i.e., the deviation from a Maxwellian is a measure of inelasticity in the particles' interactions with waves and/or turbulence.[23] Further, as previously discussed, $\sim$80.5% of the core VDFs modeled with a symmetric bi-self-similar function had exponents satisfying $2.0 \leqslant s_{ec} \leqslant 2.05$. Therefore, the majority of the core electron VDFs would be visually indistinguishable from a bi-Maxwellian, which supports previous work that used thermal distributions to model the core (e.g., Feldman et al. 1979a, 1979b) and work that found evidence for collisional effects in the core distribution (e.g., Salem et al. 2003; Bale et al. 2013).

The κ_{ec} seem to correlate with $\langle M_f \rangle_{\rm up}$, which may suggest a shock strength dependence on the shape of the upstream electron VDFs. In contrast with expectations from a dependence on quasi-static fields, the values of p_{es} are higher for quasi-parallel shocks, while q_{es} are higher for quasi-perpendicular shocks, yet neither depends on $\langle M_f \rangle_{\rm up}$.

Somewhat surprisingly, the values of κ_{eh} are larger downstream than upstream, and they increase with increasing $\langle M_f \rangle_{\rm up}$. That is, the halo spectra are softer downstream and near strong shocks. Quasi-parallel shocks, however, correlate with smaller κ_{eh}, i.e., harder halo spectra. Generally, quasi-parallel shocks are predicted to be more efficient particle accelerators for suprathermal ions and very energetic electrons[24] (e.g., Caprioli & Spitkovsky 2014), but electrons in the halo energy range are predicted to be energized the most efficiently at shocks satisfying $\theta_{Bn} > 80°$ (e.g., Park et al. 2013).

Unlike the halo, κ_{eb} are smaller near high Mach number shocks than near low Mach number shocks. The difference is likely a twofold consequence of the combined effects from shock-accelerated foreshock electrons and the method used to fit the distributions. That is, the beam/strahl component is always fit to the antisunward, field-aligned side of the VDF, while the halo is fit to the opposite. For nearly all IP shocks at 1 au, the shock normal is antisunward in a direction that would

---

[22] That is, the particle kinetic energy may not be preserved through the interaction even if the wave kinetic energy is conserved.

[23] It is also worth noting that a finite time correlation included in wave–particle interactions, something missing from quasi-linear theory, can yield a similar VDF profile (work in progress by coauthors).

[24] Suprathermal is defined here for ions in the several to tens of keV energy range, while the electrons are many tens to hundreds of keV for typical 1 au solar wind collisionless shocks.

be aligned with the nominal, ambient beam/strahl electron component. For both the halo and beam/strahl, the ratios of $\langle\kappa_{eh}\rangle_{dn}/\langle\kappa_{eh}\rangle_{up}$ and $\langle\kappa_{eb}\rangle_{dn}/\langle\kappa_{eb}\rangle_{up}$ increase with increasing $\langle M_f\rangle_{up}$. That is, the downstream halo and beam/strahl spectra are softer than the upstream for stronger shocks. Again, this is likely a consequence of the foreshock electrons that are not observed upstream of weak shocks. The details of the electron component velocity moments and associated changes will be discussed further in Papers II and III.

In summary, the first part of this three-part study presented the first statistical study to find that the core electron distribution is better fit to a self-similar VDF than a bi-Maxwellian under all conditions. This is an important result for kinetic theory and solar wind evolution. This work also provides the methodology and details necessary to reproduce and qualify the results of the nonlinear least-squares fitting performed herein. In Papers II and III, the statistical and analysis results of the velocity moments will be presented in detail. These observations are relevant for comparisons with astrophysical plasmas like the intra-galaxy-cluster medium, and they provide a statistical baseline of electron parameters near collisionless shocks for the recent *Parker Solar Probe* and upcoming *Solar Orbiter* missions.

Appendix A
Definitions and Notation

In this appendix we define the symbols and notation used throughout. In the following, for all direction-dependent parameters we use the subscript j to represent the direction, where $j = $ tot for the entire distribution, $j = \parallel$ for the parallel direction, and $j = \perp$ for the perpendicular direction. Note that parallel and perpendicular are with respect to the quasi-static magnetic field vector, B_o (nT). The generic subscript s is used to denote the particle species (e.g., electrons, protons) or the component of a single particle species (e.g., electron core). For the electron components, the subscript will be $s = ec$ for the core, $s = eh$ for the halo, $s = eb$ for the beam/strahl, $s = $ eff

for the effective population, and $s = e$ for the total/entire population. Below are the symbol/parameter definitions:

(a) *one-variable statistics*
  (a) $X_{\min} \equiv$ minimum
  (b) $X_{\max} \equiv$ maximum
  (c) $\bar{X} \equiv$ mean
  (d) $\tilde{X} \equiv$ median
  (e) $X_{25\%} \equiv$ lower quartile
  (f) $X_{75\%} \equiv$ upper quartile

(b) *fundamental parameters*
  (a) $\varepsilon_o \equiv$ permittivity of free space
  (b) $\mu_o \equiv$ permeability of free space
  (c) $c \equiv$ speed of light in vacuum (km s^{-1}) $= (\varepsilon_o\,\mu_o)^{-1/2}$
  (d) $k_B \equiv$ the Boltzmann constant (J K^{-1})
  (e) $e \equiv$ the fundamental charge (C)

(c) *plasma parameters*
  (a) $n_s \equiv$ the number density (cm^{-3}) of species s
  (b) $m_s \equiv$ the mass (kg) of species s
  (c) $Z_s \equiv$ the charge state of species s
  (d) $q_s \equiv$ the charge (C) of species $s = Z_s e$
  (e) $T_{s,j} \equiv$ the scalar temperature (eV) of the jth component of species s
  (f) $(T_{s'}/T_s)_j \equiv$ the temperature ratio (N/A) of species s and s' of the jth component
  (g) $(T_\perp/T_\parallel)_s \equiv$ the temperature anisotropy (N/A) of species s
  (h) $V_{Ts,j} \equiv$ the most probable thermal speed (km s^{-1}) of a one-dimensional velocity distribution (see Equation (6c))
  (i) $v_{os} \equiv$ the drift velocity (km s^{-1}) of species s in the plasma bulk flow rest frame
  (j) $C_s \equiv$ the sound or ion-acoustic sound speed (km s^{-1}) (see the Supplemental PDF in Wilson et al. 2019c for definitions)
  (k) $V_A \equiv$ the Alfvén speed (km s^{-1}) (see the Supplemental PDF in Wilson et al. 2019c for definitions)
  (l) $V_f \equiv$ the fast mode speed (km s^{-1}) (see the Supplemental PDF in Wilson et al. 2019c for definitions)
  (m) $\Omega_{cs} \equiv$ the angular cyclotron frequency (rad s^{-1}) (see Equation 6(d))
  (n) $\omega_{ps} \equiv$ the angular plasma frequency (rad s^{-1}) (see Equation 6(e))
  (o) $\lambda_{De} \equiv$ the electron Debye length (m) (see Equation 6(f))
  (p) $\rho_{cs} \equiv$ the thermal gyroradius (km) (see Equation 6(g))
  (q) $\lambda_s \equiv$ the inertial length (km) (see Equation 6(h))
  (r) $\beta_{s,j} \equiv$ the plasma beta (N/A) of the jth component of species s (see Equations 6(i) and 6(j))
  (s) $\phi_{sc} \equiv$ the scalar, quasi-static spacecraft potential (eV) (e.g., Scime et al. 1994b; Pulupa et al. 2014a)
  (t) $E_{\min} \equiv$ the minimum energy bin midpoint value (eV) of an electrostatic analyzer (see, e.g., Appendices in Wilson et al. 2017, 2018).

The variables that rely on multiple parameters are given in the following equations:

$$T_{\mathrm{eff},j} = \frac{\sum_s n_s\, T_{s,j}}{\sum_s n_s} \tag{6a}$$

$$T_{s,\mathrm{tot}} = \frac{1}{3}(T_{s,\parallel} + 2\,T_{s,\perp}) \tag{6b}$$

$$V_{Ts,j} = \sqrt{\frac{2 \, k_B \, T_{s,j}}{m_s}} \tag{6c}$$

$$\Omega_{cs} = \frac{q_s \, B_o}{m_s} \tag{6d}$$

$$\omega_{ps} = \sqrt{\frac{n_s \, q_s^2}{\varepsilon_o \, m_s}} \tag{6e}$$

$$\lambda_{De} = \frac{V_{Te,\text{tot}}}{\sqrt{2} \, \omega_{pe}} = \sqrt{\frac{\varepsilon_o \, k_B \, T_{e,\text{tot}}}{n_e \, e^2}} \tag{6f}$$

$$\rho_{cs} = \frac{V_{Ts,\text{tot}}}{\Omega_{cs}} \tag{6g}$$

$$\lambda_s = \frac{c}{\omega_{ps}} \tag{6h}$$

$$\beta_{s,j} = \frac{2\mu_o n_s k_B T_{s,j}}{|\boldsymbol{B}_o|^2} \tag{6i}$$

$$\beta_{\text{eff},j} = \frac{2\mu_o n_e k_B T_{\text{eff},j}}{|\boldsymbol{B}_o|^2}, \tag{6j}$$

where n_e is defined as

$$n_e = \sum_s n_{es}. \tag{6k}$$

For the macroscopic shock parameters, the values are averaged over asymptotic regions away from the shock transition region.

(a) *shock parameters*
   (a) subscripts *up* and *dn* ≡ denote the upstream (i.e., before the shock arrives timewise at the spacecraft for a forward shock) and downstream (i.e., the shocked region)
   (b) $\langle Q \rangle_j \equiv$ the average of parameter Q over the jth shock region, where $j = up$ or dn
   (c) $\boldsymbol{n}_{\text{sh}} \equiv$ the shock normal unit vector (N/A)
   (d) $\theta_{Bn} \equiv$ the shock normal angle (deg), defined as the acute reference angle between $\langle \boldsymbol{B}_o \rangle_{\text{up}}$ and $\boldsymbol{n}_{\text{sh}}$
   (e) $\langle |V_{\text{shn}}| \rangle_j \equiv$ the jth region average shock normal speed (km s^{-1}) in the spacecraft frame
   (f) $\langle |U_{\text{shn}}| \rangle_j \equiv$ the jth region average shock normal speed (km s^{-1}) in the shock rest frame (i.e., the speed of the flow relative to the shock)
   (g) $\langle M_A \rangle_j \equiv$ the jth region average Alfvénic Mach number (N/A) $= \langle |U_{\text{shn}}| \rangle_j / \langle V_A \rangle_j$
   (h) $\langle M_f \rangle_j \equiv$ the jth region average fast mode Mach number (N/A)
   (i) $M_{\text{cr}} \equiv$ the first critical Mach number (N/A)
   (j) $M_{ww} \equiv$ the linear whistler (phase) Mach number (N/A)
   (k) $M_{\text{gr}} \equiv$ the linear whistler (group) Mach number (N/A)
   (l) $M_{\text{nw}} \equiv$ the nonlinear whistler Mach number

The critical Mach numbers are phenomenologically defined as follows: for $\langle M_f \rangle_{\text{up}} / M_{\text{cr}} \geqslant 1$ an ion sound wave could not phase stand within the shock ramp (e.g., Edmiston & Kennel 1984; Kennel et al. 1985), for $\langle M_f \rangle_{\text{up}} / M_{ww} \geqslant 1$ a linear magnetosonic whistler cannot phase stand upstream of the shock ramp (e.g., Krasnoselskikh et al. 2002), for $\langle M_f \rangle_{\text{up}} / M_{\text{gr}} \geqslant 1$ a linear

magnetosonic whistler cannot group stand upstream of the shock ramp, and for $\langle M_f \rangle_{\text{up}} / M_{\text{nw}} \geqslant 1$ a nonlinear magnetosonic whistler is no longer stable/stationary and will result in the shock ramp "breaking" and reforming.

These definitions are used throughout.

Appendix B
Spacecraft Potential and Detector Calibration

The electron electrostatic analyzer data suffer from several sources of uncertainty, including differences between the theoretical maximum detector efficiency and actual (e.g., Bordoni 1971; Goruganthu & Wilson 1984), unknowns regarding the detector dead time[25] (e.g., Schecker et al. 1992; Meeks & Siegel 2008), and an unknown spacecraft potential (e.g., Scime et al. 1994a, 1994b; Pulupa et al. 2014a; Lavraud & Larson 2016). Significant advances in understanding the response and calibration of electrostatic analyzers have been made in recent years with the development and launch of the *Magnetospheric Multiscale* (*MMS*) mission (e.g., Gershman et al. 2016, 2017; Pollock et al. 2016). However, the improvements resulted from an exhaustive ground calibration campaign that most other missions, including *Wind*, have not had. Further, the electronic dead time[26] of the EESA Low preamp (i.e., AMPTEK A111) depends on the pulse height distribution of the previous pulse (J. P. McFaddon 2019, personal communication, 2011 July 18).

Although the corrections for microchannel plate (MCP) degradation, etc., have not been updated since very early in the mission, the last calibrations were performed well after the initial and most dramatic scrubbing phase that occurs when the instrument is in space (see, e.g., McFadden et al. 2008a, 2008b, for further discussions of MCP degradation over time). The currently used calibrations are those from optical geometric factor corrections, on-ground calibrations, and in-flight calibrations (D. Larson 2019, personal communication, 2011 July 18). Although there are expected to be corrections to these calibration values over the course of the time span examined in this work, the same data in the same time range have been presented in numerous refereed publications (including, but not limited to, Salem et al. 2001, 2003; Wilson et al. 2009, 2010, 2012, 2013a, 2013b, 2018; Bale et al. 2013; Pulupa et al. 2014a, 2014b). Updating the calibration tables is beyond the scope of this work but is actively being pursued (C. S. Salem et al. 2019, in preparation).

Although the *Wind* spacecraft has the capacity to measure electric fields (Bougeret et al. 1995), it does not measure the DC-coupled spacecraft potential, ϕ_{sc}. It does, however, consistently observe the upper hybrid line (also called the plasma line), which provides an unambiguous measure of the total electron density, n_e. For instance, the *Wind*/SWE Faraday cups (FCs; Ogilvie et al. 1995) are calibrated to these measurements assuming $n_e = n_p + 2n_\alpha$. Ions are generally not significantly affected by ϕ_{sc}, as they typically have $\sim$1 keV of bulk kinetic energy in the solar wind.

To estimate ϕ_{sc}, an initial guess is determined numerically from the ion density. The value of ϕ_{sc} is then adjusted until

---

[25] The dead time is the time period when the detector is unable to measure incident particles owing to the channel's discharge recovery time (i.e., time to replenish electrons to wall of conductive material in the microchannel plate), preamp cycle rates, etc.
[26] The cycle rate or sample rate of this preamp is listed as 2 MHz, but it is not constant.

Table 3
Spacecraft Potential Statistics

ϕ_{sc} (eV)	X_{min} [a]	X_{max}	$\bar{X}$	$\tilde{X}$	$X_{25\%}$	$X_{75\%}$
All: 15,144 finite values	1.01	26.7	7.05	6.70	5.45	7.84
Upstream only: 6511 finite values	1.01	26.7	7.14	6.80	5.34	7.82
Downstream only: 8633 finite values	1.92	24.8	6.43	6.45	4.00	7.37
$\langle M_f \rangle_{up} < 3$ only: 12,932 finite values	1.01	26.7	6.99	6.61	5.44	7.70
$\langle M_f \rangle_{up} \geqslant 3$ only: 2212 Finite Values	3.58	12.0	7.35	6.90	5.50	9.63
$\theta_{Bn} > 45°$ only: 10,894 finite values	1.01	26.7	6.70	6.49	5.35	7.38
$\theta_{Bn} \leqslant 45°$ only: 4250 finite values	3.53	17.6	7.94	7.14	6.10	10.2

Note. For symbol definitions, see Appendix A.
[a] Header symbols match those of Table 2.

$n_e = n_{ec} + n_{eh} + n_{eb}$ from the fits roughly equals[27] $n_p + 2n_\alpha$ and/or when photoelectrons disappear from the VDF plots.[28] Once a reliable estimate of ϕ_{sc} is determined for each VDF for each IP shock, the software is cycled through all VDFs for that event and the data are saved. This process is repeated for each IP shock event. An example time series of ϕ_{sc} is shown in Figure 3.

Note that the values of ϕ_{sc} determined above should not be treated as the absolute or correct spacecraft potential values. The reason is that the detector efficiency and gain calibrations suffer from the issues discussed above (e.g., Bordoni 1971; Goruganthu & Wilson 1984). Therefore, the ϕ_{sc} values are proxies for the spacecraft potential that comprise a complicated nonlinear convolution of the real spacecraft potential and the detector dead time and efficiency. Despite this uncertainty, the ϕ_{sc} values estimated herein are consistent with those in previously published work on the same data set within the same time span (e.g., Bale et al. 2013; Pulupa et al. 2014a). Further, the consistency checks discussed in Section 3.3 provide further validation of the fit results.
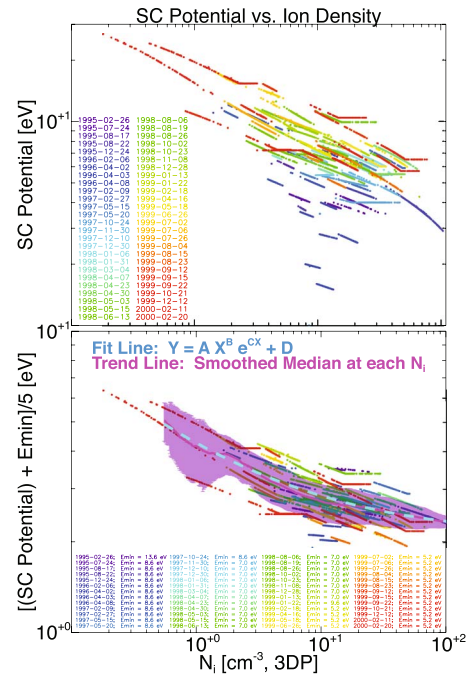
Table 3 provides the one-variable statistics of the ϕ_{sc} values for all VDFs, as well as upstream and downstream only, low and high Mach number only, and quasi-parallel and quasi-perpendicular only periods. There are no dramatic differences other than that the values of ϕ_{sc} are slightly smaller downstream than upstream, slightly higher for high than low Mach number shocks, and largest (by mean, median, and quartiles) for quasi-parallel shocks.

Figure 9 shows ϕ_{sc} versus n_i as both the raw values and a renormalized version where the EESA Low detector E_{min} is used as an offset. The data were fit to a power-law-exponential, $Y = X^B e^{CX} + D$, where $Y = (\phi_{sc} + E_{min})/5$ (eV) and $X = n_i$ (cm^{-3}). The fit parameters producing the cyan dashed line are $A = 2.272 \pm 0.013$ (cm^{+3B}), $B = -0.431 \pm 0.019$ (N/A), $C = 0.00115 \pm 0.00155$ (cm^{+3}), and $D = 2.0 \pm 0.0$ (eV), with a reduced chi-squared value of $\tilde{\chi}^2 \sim 0.144$.

The choice of the form of the fit line is empirical and matches the observations in trend. The typical approach is to measure the spacecraft potential and number density and then fit to a function of the spacecraft potential for the number density, i.e., $n_i = n_i(\phi_{sc})$ (e.g., Scudder et al. 2000). As previously stated, Wind cannot actively measure ϕ_{sc}, and the

Figure 9. Spacecraft potential, ϕ_{sc}, shown vs. the total ion density, n_i, observed by the Wind/3DP ion electrostatic analyzer (PESA Low). The top panel shows the value of ϕ_{sc} (eV) determined iteratively, as described in this appendix, vs. n_i (cm^{-3}), where the color code is defined by the IP shock data given in the lower left corner. The bottom panel shows the same data, but now ϕ_{sc} is offset by the detector minimum energy, E_{min}, and divided by the constant 5.0 to keep the magnitudes near unity. The E_{min} are color-coded and date-specific, as in the top panel. The solid magenta line is a smoothed median trend line, and the magenta shaded region indicates the standard deviation of the values at each n_i. The cyan dashed line indicates a fit line to the data using the model function defined near the top center of this panel.

values shown in Figure 9 are really a proxy owing to the uncertain values for the dead time and efficiency for each detector anode. The purpose of the above approach is to find a semianalytical expression for ϕ_{sc} that only depends on n_i (or n_e) as an initial estimate. The unexpected result here is that the trend depends on E_{min} as an offset, which is likely only reflecting a one-sided measurement boundary, preventing the detector from observing the entire VDF.

Note that similar analysis on the same data set has also found a small dipolar correction to the typical monopolar approximation used herein (e.g., Pulupa et al. 2014a). The dipole term is typically less than 1 eV, however, and only $\sim 1.5\%$ of all the VDFs examined in our study satisfied $\phi_{sc} < 1.5$ eV. Further,

---

[27] Note that the value of n_e for a constraint is taken from SWE and the upper hybrid line observed by the WAVES radio receiver (Bougeret 1995), when possible.
[28] When ϕ_{sc} is too low, a discontinuous "spike" appears in the cuts of the VDF. The spike-like feature can also be seen in 1D energy spectra shown in the spacecraft frame with no adjustment for ϕ_{sc}.

the dipole correction will only affect the odd velocity moments, i.e., the drift velocity and heat flux. We did not calculate the heat flux, but we did observe perpendicular core velocity drifts previously shown to be affected by the dipole correction (e.g., Pulupa et al. 2014a).

Appendix C
Numerical Analysis Procedure

The data are fit to a user-defined model function using the nonlinear least-squares fit algorithm called the LMA (Moré 1978). The generalized LMA software, called MPFIT (Markwardt 2009), requires at minimum the following inputs when fitting to a two-dimensional array of data:

FUNC: a scalar [string] defining the model function routine file name;

X(Y): N(M)-element [numeric] array defining the first (second) dimension coordinate abscissa values;

Z: NxM-element [numeric] array defining the dependent data associated with *X* and *Y* abscissa values;

ERR: NxM-element [numeric] array defining the error associated with each element of *Z*; and

PARAM: K-element [numeric] array defining the initial guesses for the fit parameters supplied to the model function routine *FUNC*.

The error array will be ignored if the user supplies an array of weights, $\mathcal{W}$. The details of the use of the software and documentation are provided by the author at https://www.physics.wisc.edu/~craigm/idl/fitting.html and in the publication Markwardt (2009).

For the purposes of finding numerical fits to electron VDFs in the solar wind, a substantial set of wrapping routines were written for use with the MPFIT libraries and can be found at https://github.com/lynnbwilsoniii/wind_3dp_pros. The wrapping software also provides detailed documentation with extensive manual pages and numerous comments throughout.

The approach used for each electron VDF is as follows:

1. The raw VDF data, $f^{(0r)}$, are retrieved as an IDL structure with the data in units of counts. A copy is created, and the data structure tag is replaced with the square root of the number of counts, $f^{(0cr)}$, i.e., Poisson statistics are assumed.

2. A unit conversion is applied to change to units of phase-space density (i.e., $cm^{-3} km^{-3} s^{+3}$), and then the energies are adjusted to account for the spacecraft potential (e.g., Salem et al. 2001; Wilson et al. 2014a, 2016) (details are discussed in Appendix B), giving $f^{(0sc)}$ and $f^{(0csc)}$.

3. Then $f^{(0sc)}$ and $f^{(0csc)}$ are transformed into the ion bulk flow rest frame (e.g., Compton & Getting 1935; Ipavich 1974) following the methods described in Wilson et al. (2016) using a relativistically correct Lorentz transformation. The data are then interpolated onto a regular grid using Delaunay triangulation in the plane defined by the quasi-static magnetic field, $\boldsymbol{B}_o$, along the horizontal and transverse components of the ion bulk flow velocity, $\boldsymbol{V}_i$, i.e., $(\boldsymbol{B}_o \times \boldsymbol{V}_i) \times \boldsymbol{B}_o$. The result is a two-dimensional gyrotropic VDF, $f^{(0)}$, and the associated Poisson errors/uncertainties, $f^{(0c)}$, both as functions of the parallel, $V_\parallel$, and perpendicular, $V_\perp$, velocity with respect to $\boldsymbol{B}_o$.

4. Numerous weighting schemes were tried, and the best results (for *Wind*/3DP) were achieved by defining $\mathcal{W} = (f^{(0c)})^{-2}$ for the weights.[29]

5. Every $f^{(0)}$ is fit to the sum of three model functions in two dimensions[30] for the core, halo, and beam/strahl components. Again, the components can be fit separately because the solar wind is a nonequilibrium, weakly collisional, kinetic gas.[31] The allowed model functions (defined in Section 3.1) are bi-Maxwellian (e.g., Kasper et al. 2006), bi-kappa (e.g., Vasyliunas 1968; Mace & Sydora 2010; Livadiotis 2015), symmetric bi-self-similar (e.g., Dum et al. 1974; Dum 1975), and asymmetric bi-self-similar (defined in Section 3.1).

   (a) It is important to note that the fit is not done for all components simultaneously. This was the initial approach but proved to require stringent constraints for nearly all fit parameters, and the software exited before all fit parameters were varied owing to numerical instabilities[32] (e.g., Liavas & Regalia 1999), discussed in Appendix D.

   (b) Thus, the core fit, $f^{(core)}$, is performed first, and then the model result is subtracted from the data to yield the first residual, $f^{(1)}$.

   (c) The halo fit, $f^{(halo)}$, is next but only to the side of $f^{(1)}$ opposite to that expected for the strahl/beam, where the latter is defined as the antisunward direction along $\boldsymbol{B}_o$. The entire two-dimensional halo fit is then subtracted from $f^{(1)}$ to yield the second residual, $f^{(2)}$, i.e., both sides are subtracted, but only one side is used for the fit.

   (d) The beam/strahl fit, $f^{(beam)}$, is last and fit to only the side of $f^{(2)}$ that is in the antisunward direction along $\boldsymbol{B}_o$.

6. Not all VDFs will have fit results for all three components. In fact, $f^{(beam)}$ is often not found either because $f^{(halo)}$ left too few finite elements in $f^{(2)}$ or for numerical instability reasons (discussed in Appendix D).

All model functions are defined with six input parameters to be varied by the LMA software in the following order: PARAM[0] is the number density, n_s (cm^{-3}); PARAM[1] and PARAM[2] are the parallel and perpendicular thermal speeds, $V_{Ts,j}$ ($km\,s^{-1}$); PARAM[3] and PARAM[4] are the parallel and perpendicular drift speeds, $V_{os,j}$ ($km\,s^{-1}$); and PARAM[5] is the function exponent. The exponent input is ignored for the bi-Maxwellian routine, as it is always 2.0 but can vary in the other routines. For the asymmetric bi-self-similar routine PARAM[4]

---

[29] Several approaches were tried for the $\mathcal{W}$ values, but the most reliable and robust was to use Gaussian weights on Poisson errors. Reliable and robust here mean that the fitting software required the fewest number of constraints and user-imposed limits to find fit parameters that well represent the observations.

[30] That is, the data are not fit to two one-dimensional cuts of a two-dimensional VDF separately, but rather both dimensions are fit simultaneously.

[31] It should also be noted that initial approaches tried to fit all electron components simultaneously but failed. Later approaches tried to fit the combination of only the core and halo simultaneously, but again the analysis was too unstable. Thus, the final approach fit to each component sequentially from core to beam/strahl.

[32] There is also an issue of threshold tests for convergence. The software allows the user to define the thresholds for various gradients in the Jacobian. If the gradient magnitudes fall below these thresholds, the software exits with a specific fit status parameter associated with the specific threshold. For numerous reasons, the initial approach of fitting to all three components simultaneously prevented accurate fit results owing to these thresholds being satisfied too early in the iteration process.

is the parallel exponent and PARAM[5] is the perpendicular exponent (see Section 3.1 for functional form).

Initial guesses are defined for all elements of PARAM that are specific to each shock event determined through an iterative trial-and-error approach. For each event, a zeroth-order guess is used on a subset of all VDFs, and the PARAM arrays for each component are adjusted accordingly to maximize the number of stable fit results for all components. Note that the PARAM arrays for each component differ depending on whether the VDF is located upstream or downstream of the shock ramp. In stronger shocks, the function used also varies (i.e., use symmetric bi-self-similar upstream and asymmetric bi-self-similar downstream).

Appendix D
Numerical Instability

The LMA software works by minimizing the chi-squared value given by

$$\chi_s^2 = \sum_{i=0}^{N-1} \sum_{j=0}^{M-1} (f_{ij,s}^{(0)} - f_{ij,s}^{(\mathrm{mod})})^2 \, |\mathcal{W}_{ij,s}|, \qquad (7)$$

where $f_s^{(\mathrm{mod})}$ is the model fit function of component s returned by the model function routine *FUNC* (see Section C), χ_s^2 is the chi-squared value of the fit of component s, and the i and j subscripts correspond to the indices of the parallel and perpendicular velocity space coordinates, respectively.

A total reduced chi-squared, $\tilde{\chi}_{\mathrm{tot}}^2$, value was also calculated for all VDFs analyzed herein. The difference in calculation is that the weights were not offset and the model function and distribution function are for the entire VDF, not the components. Further, unlike the components, the $\tilde{\chi}_{\mathrm{tot}}^2$ values used all data points in $f^{(0)}$ and $\mathcal{W}$ even if they were excluded during the fit process.[33] However, the $\tilde{\chi}_{\mathrm{tot}}^2$ calculation excluded data below the nine-count level to avoid non-Gaussian weights in low-count values and removed "spiky" solutions in the beam or halo fits defined by small $T_{es,j}$ and κ_{es}. That is, "spiky" solutions are defined as those satisfying $(\kappa_{es} \leqslant 3) \wedge ((T_{es,\parallel} \leqslant 11.8) \vee (T_{es,\perp} \leqslant 11.8))$ for model fit parameters. As evidenced by Figures 4–6, the $\tilde{\chi}_{\mathrm{tot}}^2$ parameter alone is not necessarily an accurate measure of the quality of the fit.

An unexpected nuance arose during the development and testing of the software. The typical phase-space density of any given element of $f^{(0)}$ for electrons near 1 au varies from $\sim 10^{-18}$ to $10^{-8}\,\mathrm{cm}^{-3}\,\mathrm{km}^{-3}\,\mathrm{s}^{+3}$. The LMA software uses a combination of gradients by constructing a Jacobian matrix of the input model fit function.[34] This is problematic when the magnitude of the input data and output model function are much much less than unity as results in numerical instabilities (e.g., Liavas & Regalia 1999). That is, the partial derivative of a number on the order of 10^{-18} with respect to a number slightly greater than unity can produce exceedingly small gradients.

While the limits of double precision are not, in general, challenged by such computations, the LMA software

(Markwardt 2009) was designed such that all the inputs are near unity. The solution was to multiply $\mathcal{W}$ by a constant offset to increase the contrast in the Jacobian components that are used to minimize χ^2. A consequence of this approach is that the output χ^2, $f^{(m)}$, and 1σ error estimates of the fit parameters must be renormalized by this offset factor. The more standard approach is to perform the fit in logarithmic space, which reduces the dynamic range of the data. However, as discussed in Appendix E, this does not necessarily produce better fit results.

The above approach worked well except for cases with so-called flat-top distributions (e.g., Feldman et al. 1983a; Thomsen et al. 1987), modeled using the self-similar distributions (e.g., Dum et al. 1974; Dum 1975; Horton et al. 1976; Horton & Choi 1979; Jain & Sharma 1979; Goldman 1984) given by either Equation (3)(a) or Equation (4)(a). In cases where the phase-space densities were independent of energy for the core, the use of the weights above was not sufficient to constrain the fits. In these cases, shock-specific constraints/limits were imposed on the least number of fit parameters necessary to reliably and robustly produce good results (see the Supplemental Material ASCII files in Wilson et al. 2019c, described in Appendix F for list of constraints by shock).

Appendix E
Numerical Method Comparisons

As stated in Appendix D, the standard approach to avoiding numerical instabilities due to the small magnitude of $f^{(0)}$ usually involves fitting to the logarithm of $f^{(0)}$ (e.g., Štverák et al. 2009). To illustrate the validity of the method used herein, an example VDF was chosen from a different study (C. J. Farrugia et al. 2019, in preparation) that examines a single shock-magnetic-cloud system.

Figure 10 shows a comparison of three different fit results to illustrate the validity of the method used herein. Given the hindsight and statistics of the results from the present analysis, more refined constraints and better initial guesses were available. The fit shown in panels (b) and (c), referred to as the *test fit* from here on, was found following the automated method used for the 52 events examined in this study, i.e., the software is given initial guesses for parameters and constraints defined by knowns like n_e and then allowed to find the best fit. The test fit results shown in panels (b) and (c) were then used as initial guesses (first perturbed, of course) on the same VDF to compare the method used herein (referred to as the *linear method*) to the base-10 logarithm approach (referred to as the *log method*). A larger range of constraints were used to provide a more open parameter space. Thus, in the following a comparison between the linear and log methods is presented as an illustrative test.

Panels (d) and (e) show the fit results using the linear method with the new initial guesses and parameter constraints, while panels (f) and (g) show the log method fit results. Unexpectedly, the log method did much worse in the core fit than the linear method but did well for the halo and beam/strahl fits. The numerical fit results are as follows:

(a) *Test Fit (Panels (b) and (c))*
   (a) $n_{ec(h)[b]} \sim 1.407(0.054)[0.060]\,\mathrm{cm}^{-3}$;
   (b) $V_{Tec(h)[b],\parallel} \sim 2028.0(3621.7)[4183.7]\,\mathrm{km\,s}^{-1}$;
   (c) $V_{Tec(h)[b],\perp} \sim 1927.2(3486.6)[2833.1]\,\mathrm{km\,s}^{-1}$;
   (d) $V_{oec(h)[b],\parallel} \sim +50.4(0.0)[-3752.6]\,\mathrm{km\,s}^{-1}$;

---

[33] Specific energy-angle bins were excluded for various physical reasons in some VDFs, including, for instance, energy and/or pitch-angle range constraints to avoid "contamination" by other components as is done to examine the halo-only and beam/strahl-only parts of the VDF.

[34] That is, the partial derivatives are with respect to the fit parameters, not velocity coordinates.
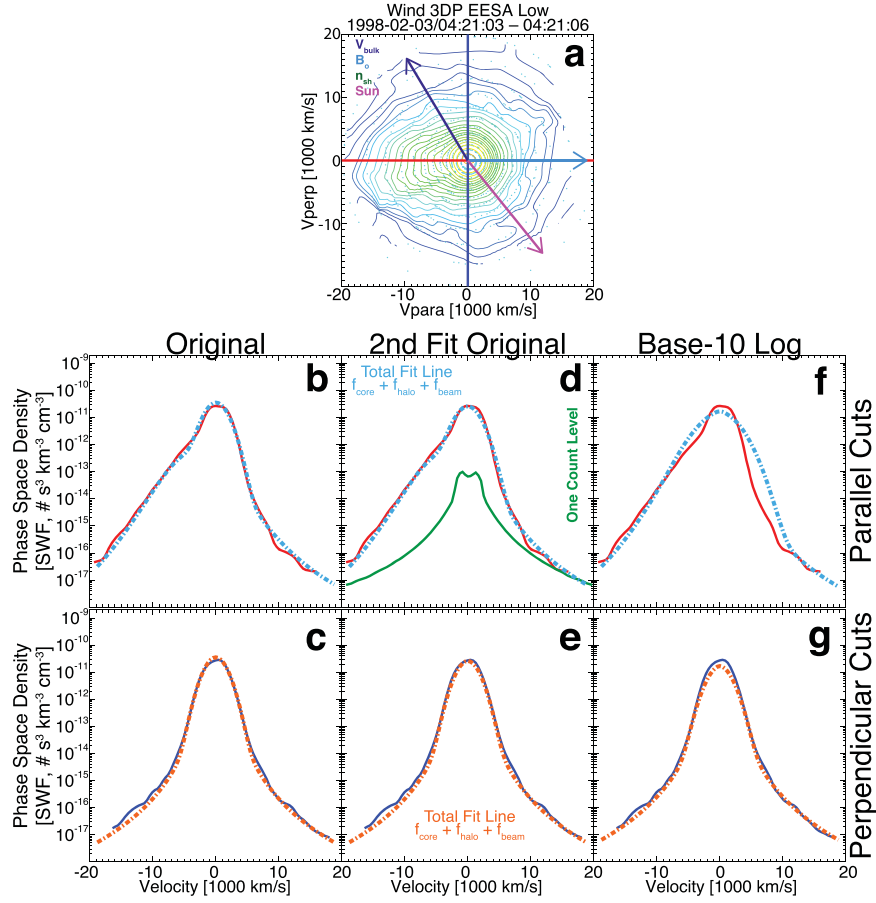
Figure 10. Example VDF observed at 04:21:03.646 UTC on 1998 February 3 by the *Wind*/3DP EESA Low detector. The format is similar to Figures [4–6](#), except that each of the one-dimensional cut panel columns shows a different fit result and only the total model fits are shown. The values of the relevant parameters for this VDF are $\boldsymbol{B}_o = (+4.59, -5.43, +1.79)$ (nT, GSE), $\boldsymbol{V}_i = (-323.98, -36.55, +30.66)$ (km s^{-1}, GSE), and $\phi_{sc} = 12.04$ eV. Panels (b), (d), and (f) show the 1D parallel cuts along the horizontal (solid red line is data in both panels), and panels (c), (e), and (g) show the 1D perpendicular cuts along the vertical (solid blue line is data in both panels). Panel (d) shows the one-count level for reference.

(e) $V_{oec(h)[b],\perp} \sim 0.0(0.0)[0.0]$ km s^{-1};
(f) $s_{ec} \sim 2.002$;
(g) $\kappa_{eh} \sim 1.908$;
(h) $\kappa_{eb} \sim 5.151$;
(i) $\delta\mathcal{R} \sim 14.1\%$;
(j) $\tilde{\chi}^2_{c(h)[b]} \sim 4.52(1.82)[2.98]$;
(k) $\tilde{\chi}^2_{tot} \sim 1.30$;
(l) Fit Flag {c,h,b} = {8, 8, 8}.

(b) *Linear Method Fit (Panels (d) and (e))*
 (a) $n_{ec(h)[b]} \sim 1.122(0.051)[0.055]$ cm^{-3};
 (b) $V_{Tec(h)[b],\parallel} \sim 2183.7(3694.7)[4154.0]$ km s^{-1};
 (c) $V_{Tec(h)[b],\perp} \sim 1947.4(3557.0)[2863.1]$ km s^{-1};
 (d) $V_{oec(h)[b],\parallel} \sim 0.0(0.0)[-3960.1]$ km s^{-1};
 (e) $V_{oec(h)[b],\perp} \sim 0.0(0.0)[0.0]$ km s^{-1};
 (f) $s_{ec} \sim 2.000$;
 (g) $\kappa_{eh} \sim 1.901$;
 (h) $\kappa_{eb} \sim 5.073$; and
 (i) $\delta\mathcal{R} \sim 12.5\%$;
 (j) $\tilde{\chi}^2_{c(h)[b]} \sim 3.73(1.82)[2.98]$;
 (k) $\tilde{\chi}^2_{tot} \sim 1.01$;
 (l) Fit Flag {c,h,b} = {8, 8, 8}.

(c) *Log Method Fit (Panels (f) and (g))*
 (a) $n_{ec(h)[b]} \sim 1.086(0.089)[0.062]$ cm^{-3};
 (b) $V_{Tec(h)[b],\parallel} \sim 3248.5(2938.9)[3762.2]$ km s^{-1};
 (c) $V_{Tec(h)[b],\perp} \sim 2086.3(3043.6)[2652.4]$ km s^{-1};

(d) $V_{oec(h)[b],\parallel} \sim 0.0(0.0)[-4206.0]$ km s^{-1};
(e) $V_{oec(h)[b],\perp} \sim 0.0(0.0)[0.0]$ km s^{-1};
(f) $s_{ec} \sim 2.000$;
(g) $\kappa_{eh} \sim 1.852$;
(h) $\kappa_{eb} \sim 4.016$;
(i) $\delta\mathcal{R} \sim 20.0\%$;
(j) $\tilde{\chi}^2_{c(h)[b]} \sim 82.7(2.51)[2.15]$;
(k) $\tilde{\chi}^2_{tot} \sim 0.71$;
(l) Fit Flag {c,h,b} = {2, 6, 6}.

Thus, one can see that the log method did not produce a better fit for this specific example, which was not the expected outcome. This is almost certainly a consequence of the large constraint ranges, and a better fit would be found for a tighter range. That is, this example is not meant to argue that the linear method is better than the log method. Rather, the example is meant to illustrate that the linear method is a viable approach.

A point should also be made about the initiation stability of the LMA software. During the course of fitting all the VDFs in the present study, it was found that the choice of initial guess parameters was critical. For instance, in the example shown in Figure [10](#), the initial guess values used for the core fit were $n_{ec} \sim 2.0$ cm^{-3}, $V_{Tec,\parallel\ [\perp]} \sim 2297$ [2297] km s^{-1} (i.e., 15 eV temperatures), $V_{oec,\parallel\ [\perp]} \sim +10.0$ [0.0] km s^{-1}, and $s_{ec} \sim 2.0$. If any of the parameters were perturbed by $\sim 20\%$–30% away from these initial guesses, the log method would not initiate fit

iterations owing to diverging deviates and/or diverging model results, i.e., the software could not establish an initial Jacobian.[35] Unexpectedly, the linear method was more tolerant of perturbed initial guess parameters. There are still several checks for each component fit to address this possible noninitiation error, but even so this sometimes did not fix the issue, which is one reason why not all VDFs had stable solutions.

Finally, a note about the 1σ uncertainties of every fit parameter. These values are not reported because it was found that they do not accurately or consistently reflect the quality of fit. For instance, the 1σ uncertainties of n_{eh} and $V_{Teh,\parallel}$ for the log method in the example VDF shown in Figure 10 (panels (f) and (g)) are $\sim$19,988 km s^{-1} (i.e., $\sim$617% error) and $\sim$3.53 cm^{-3} (i.e., $\sim$5163% error), respectively, even though $\tilde{\chi}_h^2 \sim 2.51$. The 1σ uncertainties for the same parameters but for the fit in panels (d) and (e) are $\sim$110.1 km s^{-1} (i.e., $\sim$3.1% error) and $\sim$0.0047 cm^{-3} (i.e., $\sim$8.5% error), and $\tilde{\chi}_h^2 \sim 1.82$. That is, the reduced chi-squared values differ by only $\sim$39%, but the 1σ uncertainties differ by hundreds to thousands of percent. The 1σ uncertainties determined by the LMA software that are assigned to the output fit parameters are not representative of the actual uncertainties. The reason is related to the orthogonal basis constructed during the qr-factorization (ultimately used to minimize $\tilde{\chi}_s^2$), which is not the same basis as that for the fit parameters. The output uncertainties thus contain nonlinear convolution of 1σ uncertainties from potentially multiple fit parameters. The effect is analogous to electric field measurements from two antennas with differing noise levels. If the electric field data are rotated to a new coordinate basis from the original instrument basis, the resulting field components will have a nonlinear convolution of noise from the original components. Thus, the 1σ uncertainties were not used as errors for each parameter.

The 1σ errors are also forced to zero in the software when the fit value reaches a user-defined boundary/constraint/limit. This is reported in the fit constraints ASCII file described in Appendix F (i.e., under the heading "Peg" in the ASCII file). As previously stated, the $\delta\mathcal{R}$ value alone does not always characterize the quality of any given fit. Therefore, a combination of parameters were used to define fit quality flags (see Appendix F for definitions), which should be used for determining the reliability of any given fit.

Appendix F
Data Product

One of the primary purposes of this first part of this three-part study is to describe the methodology and nuances of the fit procedure to provide context and documentation for the resulting data product (Wilson et al. 2019c). This will serve as the reference document for use of the data product by the heliospheric and astrophysical communities. The nuances and details of the procedure are critical for reproducibility and quality control in the use of the data product described in this section. While Papers II and III discuss the statistics and analysis results in detail, this first part is critical for any statistical or physical interpretation of the data, and it includes analysis of the exponents and drifts.

The fit results are provided in two ASCII files. The first contains all fit parameters for the three electron components in addition to several other relevant parameters. The nonelectron data products are linearly interpolated to the midpoint time stamp of each electron VDF. The ASCII file contains a detailed header with descriptions and explanations of the parameters with associated units. The data included are as follows: UTC time of electron VDF midpoint time stamp; n_p and n_α measured by SWE (cm^{-3}); n_i measured by 3DP (cm^{-3}); $T_{p,j}$ and $T_{\alpha,j}$ measured by SWE (eV); $T_{i,j}$ measured by 3DP (eV); $B_{o,j}$ measured by MFI (nT); $V_{p,j}$ and $V_{\alpha,j}$ measured by SWE (km s^{-1}); $V_{i,j}$ measured by 3DP (km s^{-1}); ϕ_{sc} determined from fit process (eV); $\delta\mathcal{R}$ calculated from fit process (%); n_{es} from 3DP fits (cm^{-3}); $T_{es,j}$ from 3DP fits (eV); $V_{oes,j}$ from 3DP fits (km s^{-1}); κ_{es}, p_{es}, and q_{es} from 3DP fits (N/A); $\tilde{\chi}_s^2$ from 3DP fits (N/A); and the numeric fit status value for each electron component (N/A). The total reduced chi-squared values for all fits are also included in the ASCII file. The fit flags for each component fit are also included. Let $\Xi \equiv \sum_s \tilde{\chi}_s^2$; then, the list is as follows:

1. Fit Flag $\{c, h, b\} = 0 : (100\% \leqslant \delta\mathcal{R}) \vee$ nonfinite for any of the following: $\Xi, \tilde{\chi}_s^2, \delta\mathcal{R}$
2. Fit Flag $\{c, h, b\} = 1 : (100 \leqslant \tilde{\chi}_{tot}^2 < 10^{30}) \wedge ((\Xi < 200) \vee (\tilde{\chi}_s^2 \leqslant 200)) \wedge (\delta\mathcal{R} < 95\%)$
3. Fit Flag $\{c, h, b\} = 2 : (0 \leqslant \tilde{\chi}_{tot}^2 < 100) \wedge ((\Xi < 100) \vee (\tilde{\chi}_s^2 \leqslant 100)) \wedge (\delta\mathcal{R} < 75\%)$
4. Fit Flag $\{c, h, b\} = 3 : (0 \leqslant \tilde{\chi}_{tot}^2 < 100) \wedge ((\Xi < 50) \vee (\tilde{\chi}_s^2 \leqslant 40)) \wedge (\delta\mathcal{R} < 55\%)$
5. Fit Flag $\{c, h, b\} = 4 : (0 \leqslant \tilde{\chi}_{tot}^2 < 100) \wedge ((\Xi < 40) \vee (\tilde{\chi}_s^2 \leqslant 30)) \wedge (\delta\mathcal{R} < 50\%)$
6. Fit Flag $\{c, h, b\} = 5 : (0 \leqslant \tilde{\chi}_{tot}^2 < 100) \wedge ((\Xi < 30) \vee (\tilde{\chi}_s^2 \leqslant 20)) \wedge (\delta\mathcal{R} < 45\%)$
7. Fit Flag $\{c, h, b\} = 6 : (0 \leqslant \tilde{\chi}_{tot}^2 < 100) \wedge ((\Xi < 20) \vee (\tilde{\chi}_s^2 \leqslant 10)) \wedge (\delta\mathcal{R} < 40\%)$
8. Fit Flag $\{c, h, b\} = 7 : (0 \leqslant \tilde{\chi}_{tot}^2 < 30) \wedge ((\Xi < 15) \vee (\tilde{\chi}_s^2 \leqslant 9)) \wedge (\delta\mathcal{R} < 30\%)$
9. Fit Flag $\{c, h, b\} = 8 : (0 \leqslant \tilde{\chi}_{tot}^2 < 30) \wedge ((\Xi < 10) \vee (\tilde{\chi}_s^2 \leqslant 7)) \wedge (\delta\mathcal{R} < 20\%)$
10. Fit Flag $\{c, h, b\} = 9 : (0 \leqslant \tilde{\chi}_{tot}^2 < 15) \wedge ((\Xi < 7) \vee (\tilde{\chi}_s^2 \leqslant 5)) \wedge (\delta\mathcal{R} < 15\%)$
11. Fit Flag $\{c, h, b\} = 10 : (0 \leqslant \tilde{\chi}_{tot}^2 < 7) \wedge ((\Xi < 5) \vee (\tilde{\chi}_s^2 \leqslant 3)) \wedge (\delta\mathcal{R} \leqslant 10\%)$.

The second ASCII file contains the fit constraints, initial guesses, whether the fit parameters reached a fit constraint boundary, the number of iterations required to reach a stable fit, the chi-squared of the fit, degrees of freedom of the inputs, and a two-letter code for the model function used.

Both ASCII files contain fit results even if they are not high-quality or reliable results, which can be determined from the combination of $\tilde{\chi}_s^2$, $\tilde{\chi}_{tot}^2$, and $\delta\mathcal{R}$ used to define the fit flags in the first ASCII file, as discussed previously. The entries with fill values (listed in the header) resulted because a stable fit was not found or the fit was determined to be "bad," as defined in Section 3.3 and Appendix C. When there is a significant discrepancy between n_p and n_i (e.g., differ by a factor exceeding $\sim$40%), the more reliable/accurate of the two is n_p. Under these circumstances, $T_{i,j}$ and $V_{i,j}$ should be subject to

---

[35] This is associated with a fit status code of -16 as reported in the fit results ASCII file discussed in Appendix F.
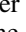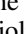
scrutiny as well. The model function used for the core is given in the second ASCII file.

Note that the second ASCII file will contain nonfill, fit values for the same parameters that are all fill values in the first ASCII file. Although many constraints were set as far from the expected values as possible to avoid a parameter from being limited during the fit, some were imposed after all the fits were found for a given shock crossing. These were imposed for physical reasons (see, e.g., Section 3.2) and to avoid issues during regridding and/or interpolation for comparison with other data sets (e.g., magnetic fields). These post-fit constraints are $1.5 < \kappa_{eh} \leqslant 20$, $1.5 < \kappa_{eb} \leqslant 20$, $0 \leqslant n_{eh}/n_{ec} \leqslant 0.75$, $0 \leqslant n_{eb}/n_{ec} \leqslant 0.50$, $0.0 \leqslant n_{eb}/n_{eh} \leqslant 3.0$, $11.4\,\mathrm{eV} \leqslant T_{eh,j} \leqslant 285\,\mathrm{eV}$, and $11.4\,\mathrm{eV} \leqslant T_{eb,j} \leqslant 285\,\mathrm{eV}$. All statistics and fit results presented herein are with respect to the first ASCII file values, but we include all the fit results in the second ASCII file for reference. This is because some of our post-fit constraints eliminated good fits like that shown in Figure 6, which failed the $n_{eb}/n_{eh} < 3$ test. Most of the fits that failed this specific test were clearly bad fits, but not all.

The purpose of providing the detailed inputs for the fit results is for reproducibility and for quality control/sanity checks for researchers in the heliospheric and astrophysical communities interested in future use of the data. The data product will benefit current and future missions like *Parker Solar Probe*, in addition to providing a statistical comparison with astrophysical shocks, which is currently not available.

ORCID iDs

Lynn B. Wilson III https://orcid.org/0000-0002-4313-1970
Li-Jen Chen https://orcid.org/0000-0002-4768-189X
Shan Wang https://orcid.org/0000-0002-6783-7759
Steven J. Schwartz https://orcid.org/0000-0003-0682-2753
Drew L. Turner https://orcid.org/0000-0002-2425-7818
Michael L. Stevens https://orcid.org/0000-0002-7728-0085
Justin C. Kasper https://orcid.org/0000-0002-7077-930X
Adnane Osmane https://orcid.org/0000-0003-2555-5953
Damiano Caprioli https://orcid.org/0000-0003-0939-8775
Stuart D. Bale https://orcid.org/0000-0002-1989-3596
Marc P. Pulupa https://orcid.org/0000-0002-1573-7457
Chadi S. Salem https://orcid.org/0000-0002-6536-1531
Katherine A. Goodrich https://orcid.org/0000-0002-4288-5084

References

Artemyev, A. V., Neishtadt, A. I., Vasiliev, A. A., & Mourenas, D. 2016, PhPl, 23, 090701
Artemyev, A. V., Neishtadt, A. I., Vasiliev, A. A., & Mourenas, D. 2017a, PhRvE, 95, 023204
Artemyev, A. V., Neishtadt, A. I., Vasiliev, A. A., & Mourenas, D. 2018, JPlPh, 84, 905840206
Artemyev, A. V., Neishtadt, A. I., Vasiliev, A. A., & Zelenyi, L. M. 2015, PhRvL, 115, 155001
Artemyev, A. V., Rankin, R., & Vasko, I. Y. 2017b, JGR, 122, 5519
Artemyev, A. V., Vasiliev, A. A., Mourenas, D., et al. 2014, GeoRL, 41, 5727
Artemyev, A. V., Vasiliev, A. A., Mourenas, D., Agapitov, O. V., & Krasnoselskikh, V. V. 2013, PhPl, 20, 122901
Bale, S. D., Pulupa, M., Salem, C., Chen, C. H. K., & Quataert, E. 2013, ApJL, 769, L22
Bale, S. D., Reiner, M. J., Bougeret, J.-L., et al. 1999, GeoRL, 26, 1573
Bordoni, F. 1971, NucIM, 97, 405
Bougeret, J.-L., Kaiser, M. L., Kellogg, P. J., et al. 1995, SSRv, 71, 231
Breneman, A., Cattell, C., Kersten, K., et al. 2013, JGR, 118, 7654
Broiles, T. W., Livadiotis, G., Burch, J. L., et al. 2016, JGR, 121, 7407
Caprioli, D., & Spitkovsky, A. 2014, ApJ, 783, 91

Chen, L.-J., Wang, S., Wilson, L. B., III, et al. 2018, PhRvL, 120, 225101
Compton, A. H., & Getting, I. A. 1935, PhRv, 47, 817
Coroniti, F. V. 1970, JPlPh, 4, 265
Crooker, N. U., Larson, D. E., Kahler, S. W., Lamassa, S. M., & Spence, H. E. 2003, GeoRL, 30, 1619
Dum, C. T. 1975, PhRvL, 35, 947
Dum, C. T., Chodura, R., & Biskamp, D. 1974, PhRvL, 32, 1231
Edmiston, J. P., & Kennel, C. F. 1984, JPlPh, 32, 429
Feldman, W. C., Anderson, R. C., Bame, S. J., et al. 1983a, JGR, 88, 96
Feldman, W. C., Anderson, R. C., Bame, S. J., et al. 1983b, JGR, 88, 9949
Feldman, W. C., Asbridge, J. R., Bame, S. J., & Gosling, J. T. 1979a, JGR, 84, 7371
Feldman, W. C., Asbridge, J. R., Bame, S. J., Gosling, J. T., & Lemons, D. S. 1978, JGR, 83, 5285
Feldman, W. C., Asbridge, J. R., Bame, S. J., Gosling, J. T., & Lemons, D. S. 1979b, JGR, 84, 4463
Feldman, W. C., Asbridge, J. R., Bame, S. J., Montgomery, M. D., & Gary, S. P. 1975, JGR, 80, 4181
Feldman, W. C., Bame, S. J., Gary, S. P., et al. 1982, PhRvL, 49, 199
Fuselier, S. A., & Gurnett, D. A. 1984, JGR, 89, 91
Gershman, D. J., Avanov, L. A., Boardsen, S. A., et al. 2017, JGR, 122, 11548
Gershman, D. J., Gliese, U., Dorelli, J. C., et al. 2016, JGR, 121, 10005
Goldman, M. V. 1984, RvMP, 56, 709
Goodrich, K. A., Ergun, R. E., Schwartz, S. J., et al. 2018, JGR, 123, 9430
Goodrich, K. A., Ergun, R. E., Schwartz, S. J., et al. 2019, JGR, 124, 1855
Goruganthu, R. R., & Wilson, W. G. 1984, RScI, 55, 2030
Graham, G. A., Rae, I. J., Owen, C. J., et al. 2017, JGR, 122, 3858
Graham, G. A., Rae, I. J., Owen, C. J., & Walsh, A. P. 2018, ApJ, 855, 40
Harten, R., & Clark, K. 1995, SSRv, 71, 23
Horaites, K., Boldyrev, S., Wilson, L. B., III, Viñas, A. F., & Merka, J. 2018, MNRAS, 474, 115
Horton, W., & Choi, D. 1979, PhR, 49, 273
Horton, W., Jr., Choi, D.-I., & Koch, R. A. 1976, PhRvA, 14, 424
Hull, A. J., Scudder, J. D., Frank, L. A., Paterson, W. R., & Kivelson, M. G. 1998, JGR, 103, 2041
Ipavich, F. M. 1974, GeoRL, 1, 149
Jain, H. C., & Sharma, S. R. 1979, BePl, 19, 19
Kasper, J. C., Lazarus, A. J., Steinberg, J. T., Ogilvie, K. W., & Szabo, A. 2006, JGR, 111, 3105
Kasper, J. C., Maruca, B. A., Stevens, M. L., & Zaslavsky, A. 2013, PhRvL, 110, 091102
Kasper, J. C., Stevens, M. L., Korreck, K. E., et al. 2012, ApJ, 745, 162
Kennel, C. F., Edmiston, J. P., & Hada, T. 1985, GMS, 34, 1
Krasnoselskikh, V. V., Lembège, B., Savoini, P., & Lobzin, V. V. 2002, PhPl, 9, 1192
Lavraud, B., & Larson, D. E. 2016, JGR, 121, 8462
Lazar, M., Fichtner, H., & Yoon, P. H. 2016, A&A, 589, A39
Lazar, M., Pierrard, V., Shaaban, S. M., Fichtner, H., & Poedts, S. 2017, A&A, 602, A44
Lazar, M., Poedts, S., & Fichtner, H. 2015a, A&A, 582, A124
Lazar, M., Poedts, S., Schlickeiser, R., & Dumitrache, C. 2015b, MNRAS, 446, 3022
Lazar, M., Shaaban, S. M., Fichtner, H., & Poedts, S. 2018, PhPl, 25, 022902
Lepping, R. P., Acuña, M. H., Burlaga, L. F., et al. 1995, SSRv, 71, 207
Liavas, A. P., & Regalia, P. A. 1999, ITSP, 47, 88
Lin, R. P. 1998, SSRv, 86, 61
Lin, R. P., Anderson, K. A., Ashford, S., et al. 1995, SSRv, 71, 125
Livadiotis, G. 2015, JGR, 120, 1607
Livadiotis, G. 2017, J. Phys. Conf. Ser., 900, 012014
Livadiotis, G., Desai, M. I., & Wilson, L. B., III 2018, ApJ, 853, 142
Mace, R. L., & Sydora, R. D. 2010, JGR, 115, 7206
Maksimovic, M., Bougeret, J.-L., Perche, C., et al. 1998, GeoRL, 25, 1265
Maksimovic, M., Pierrard, V., & Riley, P. 1997, GeoRL, 24, 1151
Maksimovic, M., Zouganelis, I., Chaufray, J.-Y., et al. 2005, JGR, 110, 9104
Malkov, M. A., & Drury, L. O. 2001, RPPH, 64, 429
Markwardt, C. B. 2009, in ASP Conf. Ser. 411, Astronomical Data Analysis Software and Systems XVIII, ed. D. A. Bohlender, D. Durand, & P. Dowler (San Francisco, CA: ASP), 251
Marsch, E., & Livi, S. 1985, PhFl, 28, 1379
Maruca, B. A., & Kasper, J. C. 2013, AdSpR, 52, 723
Maruca, B. A., Kasper, J. C., & Bale, S. D. 2011, PhRvL, 107, 201101
Masters, A., Schwartz, S. J., Henley, E. M., et al. 2011, JGR, 116, A10
Matyka, M., Gołembiewski, J., & Koza, Z. 2016, PhRvE, 93, 013110
McFadden, J. P., Carlson, C. W., Larson, D., et al. 2008a, SSRv, 141, 277
McFadden, J. P., Carlson, C. W., Larson, D., et al. 2008b, SSRv, 141, 477
Meeks, C., & Siegel, P. B. 2008, AmJPh, 76, 589

Moré, J. J. 1978, LNM, 630, 105
Morse, R. L. 1965, PhFl, 8, 308
Nicolaou, G., Livadiotis, G., Owen, C. J., Verscharen, D., & Wicks, R. T. 2018, ApJ, 864, 3
Nieves-Chinchilla, T., & Viñas, A. F. 2008, JGR, 113, A02105
Ogilvie, K. W., Chornay, D. J., Fritzenreiter, R. J., et al. 1995, SSRv, 71, 55
Ogilvie, K. W., Fitzenreiter, R., & Desch, M. 2000, JGR, 105, 27277
Owens, M. J., Lockwood, M., Riley, P., & Linker, J. 2017, JGR, 122, 10980
Pagel, C., Crooker, N. U., Larson, D. E., Kahler, S. W., & Owens, M. J. 2005, JGR, 110, 1103
Pagel, C., Gary, S. P., de Koning, C. A., Skoug, R. M., & Steinberg, J. T. 2007, JGR, 112, 4103
Park, J., Caprioli, D., & Spitkovsky, A. 2015, PhRvL, 114, 085003
Park, J., Ren, C., Workman, J. C., & Blackman, E. G. 2013, ApJ, 765, 147
Paschmann, G., & Daly, P. W. 1998, ISSIR, 1
Phillips, J. L., Gosling, J. T., McComas, D. J., et al. 1989a, JGR, 94, 6563
Phillips, J. L., Gosling, J. T., McComas, D. J., Bame, S. J., & Smith, E. J. 1989b, JGR, 94, 13377
Pierrard, V., Lazar, M., Poedts, S., et al. 2016, SoPh, 291, 2165
Pierrard, V., Lazar, M., & Schlickeiser, R. 2011, SoPh, 269, 421
Pierrard, V., Maksimovic, M., & Lemaire, J. 1999, JGR, 104, 17021
Pierrard, V., Maksimovic, M., & Lemaire, J. 2001, Ap&SS, 277, 195
Pilipp, W. G., Muehlhaeuser, K., Miggenrieder, H., Rosenbauer, H., & Schwenn, R. 1990, JGR, 95, 6305
Pilipp, W. G., Muehlhaeuser, K.-H., Miggenrieder, H., Montgomery, M. D., & Rosenbauer, H. 1987a, JGR, 92, 1075
Pilipp, W. G., Muehlhaeuser, K.-H., Miggenrieder, H., Montgomery, M. D., & Rosenbauer, H. 1987b, JGR, 92, 1093
Pilipp, W. G., Muehlhaeuser, K.-H., Miggenrieder, H., Rosenbauer, H., & Schwenn, R. 1987c, JGR, 92, 1103
Pollock, C., Moore, T., Jacques, A., et al. 2016, SSRv, 199, 331
Pulupa, M., & Bale, S. D. 2008, ApJ, 676, 1330
Pulupa, M. P., Bale, S. D., & Kasper, J. C. 2010, JGR, 115, 4106
Pulupa, M. P., Bale, S. D., Salem, C., & Horaites, K. 2014a, JGR, 119, 647
Pulupa, M. P., Salem, C., Phan, T. D., Gosling, J. T., & Bale, S. D. 2014b, ApJL, 791, L17
Saeed, S., Sarfraz, M., Yoon, P. H., Lazar, M., & Qureshi, M. N. S. 2017, MNRAS, 465, 1672
Sagdeev, R. Z. 1966, RvPP, 4, 23
Saito, S., & Gary, S. P. 2007, JGR, 112, 6116
Saito, S., Gary, S. P., Li, H., & Narita, Y. 2008, PhPl, 15, 102305
Salem, C., Bosqued, J.-M., Larson, D. E., et al. 2001, JGR, 106, 21701
Salem, C., Hubert, D., Lacombe, C., et al. 2003, ApJ, 585, 1147
Schecker, J. A., Schauer, M. M., Holzscheiter, K., & Holzscheiter, M. H. 1992, NIMPA, 320, 556
Schunk, R. W. 1975, P&SS, 23, 437
Schunk, R. W. 1977, RvGSP, 15, 429
Schwartz, S. J., & Marsch, E. 1983, JGR, 88, 9919
Schwartz, S. J., Thomsen, M. F., Bame, S. J., & Stansberry, J. 1988, JGR, 93, 12923
Scime, E. E., Bame, S. J., Feldman, W. C., et al. 1994a, JGR, 99, 23401
Scime, E. E., Phillips, J. L., & Bame, S. J. 1994b, JGR, 99, 14769
Scudder, J. D., Cao, X., & Mozer, F. S. 2000, JGR, 105, 21281

Shaaban, S. M., Lazar, M., & Poedts, S. 2018, MNRAS, 480, 310
Shizgal, B. D. 2018, PhRvE, 97, 052144
Skoug, R. M., Feldman, W. C., Gosling, J. T., McComas, D. J., & Smith, C. W. 2000, JGR, 105, 23069
Štverák, v., Maksimovic, M., Trávníček, P. M., et al. 2009, JGR, 114, 5104
Štverák, v., Trávníček, P., Maksimovic, M., et al. 2008, JGR, 113, 3103
Tao, J., Wang, L., Zong, Q., et al. 2016a, in AIP Conf. Ser. 1720, SOLAR WIND 14, ed. L. Wang et al. (Melville, NY: AIP), 070006
Tao, J., Wang, L., Zong, Q., et al. 2016b, ApJ, 820, 22
Thomsen, M. F., Gosling, J. T., Bame, S. J., & Mellott, M. M. 1985, JGR, 90, 137
Thomsen, M. F., Gosling, J. T., Onsager, T. G., & Russell, C. T. 1993, JGR, 98, 3875
Thomsen, M. F., Stansberry, J. A., Bame, S. J., Gosling, J. T., & Mellott, M. M. 1987, JGR, 92, 10119
Tidman, D. A., & Krall, N. A. 1971, Shock Waves in Collisionless Plasmas (New York: Wiley)
Treumann, R. A. 2009, A&ARv, 17, 409
Trotta, D., & Burgess, D. 2019, MNRAS, 482, 1154
Van Kampen, N. G. 1969, Phy, 43, 244
Vasyliunas, V. M. 1968, JGR, 73, 2839
Viñas, A. F., Gurgiolo, C., Nieves-Chinchilla, T., Gary, S. P., & Goldstein, M. L. 2010, in Proc. AIP Conf. Ser. 1216, 12th SOLAR WIND Conf., ed. M. Maksimovic et al. (Melville, NY: AIP), 265
Vocks, C., & Mann, G. 2003, ApJ, 593, 1134
Vocks, C., Salem, C., Lin, R. P., & Mann, G. 2005, ApJ, 627, 540
Wang, L., Lin, R. P., Salem, C., et al. 2012, ApJL, 753, L23
Wang, L., Yang, L., He, J., et al. 2015, ApJL, 803, L2
Wicks, R. T., Alexander, R. L., Stevens, M. L., et al. 2016, ApJ, 819, 6
Wilson, L. B., III 2016, GMS, 216, 269
Wilson, L. B., III, Cattell, C., Kellogg, P. J., et al. 2007, PhRvL, 99, 041101
Wilson, L. B., III, Cattell, C. A., Kellogg, P. J., et al. 2009, JGR, 114, 10106
Wilson, L. B., III, Cattell, C. A., Kellogg, P. J., et al. 2010, JGR, 115, 12104
Wilson, L. B., III, Chen, L.-J., Wang, S., et al. 2019a, ApJ, submitted
Wilson, L. B., III, Chen, L.-J., Wang, S., et al. 2019b, ApJ, submitted
Wilson, L. B., III, Chen, L.-J., Wang, S., et al. 2019c, Supplement to: Electron Energy Partition across Interplanetary Shocks v.1.0, Zenodo, doi:10.5281/zenodo.2875806
Wilson, L. B., III, Koval, A., Sibeck, D. G., et al. 2013a, JGR, 118, 957
Wilson, L. B., III, Koval, A., Szabo, A., et al. 2012, GeoRL, 39, 8109
Wilson, L. B., III, Koval, A., Szabo, A., et al. 2013b, JGR, 118, 5
Wilson, L. B., III, Koval, A., Szabo, A., et al. 2017, JGR, 122, 9115
Wilson, L. B., III, Sibeck, D. G., Breneman, A. W., et al. 2014a, JGR, 119, 6455
Wilson, L. B., III, Sibeck, D. G., Breneman, A. W., et al. 2014b, JGR, 119, 6475
Wilson, L. B., III, Sibeck, D. G., Turner, D. L., et al. 2016, PhRvL, 117, 215101
Wilson, L. B., III, Stevens, M. L., Kasper, J. C., et al. 2018, ApJS, 236, 41
Wu, C. S. 1984, JGR, 89, 8857
Yoon, P. H. 2014, JGR, 119, 7074
Yoon, P. H., Hong, J., Kim, S., et al. 2012, ApJ, 755, 112
Yoon, P. H., Kim, S., & Choe, G. S. 2015, ApJ, 812, 169
Yoon, P. H., Kim, S., Choe, G. S., & moon, Y.-J 2016, ApJ, 826, 204